Chapter 9
Nanoscale Phononic Crystals and Structures

N. Swinteck, Pierre A. Deymier, K. Muralidharan, and R. Erdmann

Abstract The objective of this chapter is to explore advances in the development of phononic crystals and phononic structures at the nanoscale. The downscaling of phononic structures to nanometric dimensions requires an atomic treatment of the constitutive materials. At the nanoscale, the propagation of phonons may not be completely ballistic (wave-like) and nonlinear phenomena such as phonon–phonon scattering occur. We apply second-order perturbation theory to a one-dimensional anharmonic crystal to shed light on phonon self-interaction and three-phonon scattering processes. We emphasize the competition between dispersion effects induced by the structure, anharmonicity of the atomic bonds, and boundary scattering. These phenomena are illustrated by several examples of atomistic models of nanoscale phononic structures simulated using the method of molecular dynamics (MD). Special attention is also paid to size effects.

9.1 Introduction

Nanofabrication techniques can be used to structure matter in a way that affects the propagation of phononic excitations such as high frequency (short wavelength) thermal phonons. Modulating the thermal properties of materials by creating a nanoscale composite structure is an approach that has been extensively studied in the case of superlattices [1–3]. These stacks of nanoscale layers have been shown experimentally and theoretically [4, 5] to impact thermal transport due to scattering effects of phonons.

N. Swinteck (✉) • P.A. Deymier • K. Muralidharan • R. Erdmann
Department of Materials Science and Engineering, University of Arizona, Tucson, AZ 85721, USA
e-mail: swinteck@email.arizona.edu; deymier@email.arizona.edu; Krishna@email.arizona.edu; fluid.thought@gmail.com

P.A. Deymier (ed.), *Acoustic Metamaterials and Phononic Crystals*,
Springer Series in Solid-State Sciences 173, DOI 10.1007/978-3-642-31232-8_9,

While superlattices are actually one-dimensional phononic structures, only a few studies have investigated 2D and 3D nanophononic structures. Most studies on 2D and 3D phononic crystals (PCs) have focused on macroscopic elastic systems. However this large body of knowledge suggests a possibility of designing dispersive properties by downscaling PCs to nanodimensions to affect the propagation characteristics of phonons with frequencies exceeding the THz range [6]. Recently, Gillet et al. [7] have reported simulations of atomic-level phononic structures made of three-dimensional lattices of Ge quantum dots in a Si matrix. They have shown a decrease of the thermal conductivity by several orders of magnitude due to the periodic structure of the system. Davis and Hussein [8] have considered three-dimensional nanoscale phononic crystals formed from silicon and cubic voids of vacuum. The voids are arranged on a simple cubic lattice with a lattice constant an order of magnitude larger than that of the bulk crystalline silicon primitive cell. This study showed that dispersion at the phononic crystal unit cell level plays a noticeable role in determining the thermal conductivity and that boundary scattering can also be a dominant factor. Control of high-frequency thermal phonons via structural periodicity requires preserving elastic Bragg scattering and is a significant challenge because of the possible loss of phonon coherence due to inherent inelastic scattering resulting from the anharmonicity of interatomic bonds. Band-structure effects will be highest at low temperatures where there is less anharmonic scattering [5] but one has to operate at often undesirably low temperatures [9]. For applications at ambient temperature and phononic crystal dimensions that can be fabricated with relative ease, the transition between Bragg- and inelastic-dominated scattering depends on the characteristic length of the phononic crystal and the Debye temperature of the constitutive material. This latter quantity relates directly to the phonon coherence length. Two-dimensional materials such as graphene or boron nitride (BN) sheets are therefore particularly suited for such applications due to their high phonon coherence length. Atomistic computational methods have been employed to shed light on the transport behavior of thermal phonons in models of graphene antidot super-lattice structures composed of periodic arrays of holes [10]. The phonon lifetime and thermal conductivity as a function of the crystal filling fraction and temperature were calculated in this study. These calculations indicated coherent phononic effects even at room temperature.

The first section of this chapter focuses on the relationship between wave interactions and dispersion in one-dimensional anharmonic crystals. This is done using second-order pertubation theory as well as numerial simulations of molecular dynamics (MD) models of nanoscale phononic systems. Details on the perturbation theory approach are given for pedagogical reasons. Subsequent sections show that coherent phononic effects due to period arrays of scatterers and/or asymmetric scatterers are achievable in nanostructured two-dimensional high-Debye temperature materials such as graphene and BN sheets. Attention is also paid to the competition between phonon–phonon scattering and boundary scattering.

9.2 Anharmonic One-Dimensional Atomic Structures

9.2.1 *Perturbation Theory of the Mono-Atomic Anharmonic Crystal*

In a harmonic crystal, the vibrational modes do not interact. Anharmonic lattice dynamics methods have been applied to introduce phonon interactions in three-dimensional crystals as perturbations to the harmonic solution [11–13]. Anharmonic forces lead to mode-dependent frequency shifts and introduce finite phonon life-time (i.e., line-width). In this section, we consider the anharmonic one-dimensional monoatomic crystal as a simple model to shed light on the effect of nonlinear interatomic forces on the vibrational modes that this medium can support. Amplitude-dependent self-interaction of a wave in a monoatomic and diatomic chain of masses and springs with nonlinear cubic forces has been studied [14]. It was shown that the dispersion curves undergo frequency shifts dependent on the amplitude of the wave. The interaction between two different waves in a nonlinear monoatomic chain results in the formation of different dispersion branches that are amplitude and frequency dependent [15]. Here, we employ second-order perturbation theory based on multiple time scale analysis [16, 17] and provide a detailed derivation of the anharmonic modes.

A schematic illustration of the 1D monoatomic crystal is shown in Fig. 9.1a. The potential energy function detailing the interaction between neighboring masses in the 1D crystal is shown in Fig. 9.1b. The parameter (ε) characterizes the strength of nonlinearity in the springs connecting the masses. As ε increases in magnitude a region of instability emerges in the potential energy function.

The equation of motion for the quadratically nonlinear monoatomic chain is represented by (9.1):

$$m\frac{\mathrm{d}^2u_n(t)}{\mathrm{d}t^2} = \beta(u_{n+1} - 2u_n + u_{n-1}) + \varepsilon\left[(u_{n+1} - u_n)^2 - (u_n - u_{n-1})^2\right], \tag{9.1}$$

where m is mass, $u_n(t)$ is the displacement from equilibrium of the nth mass, β is linear stiffness, and ε is a small parameter characterizing quadratic nonlinearity. The time variable (t) is replaced by a collection of variables $\tau = (\tau_0, \tau_1, \tau_2)$ whereby: $\tau_0 = t$, $\tau_1 = \varepsilon t$, $\tau_2 = \varepsilon^2 t$. Under this condition, (9.1) becomes

$$\frac{\mathrm{d}^2u_n(\tau_0, \tau_1, \tau_2)}{\mathrm{d}t^2} = {\omega_n}^2(u_{n+1} - 2u_n + u_{n-1}) + \frac{\varepsilon}{m}\left[(u_{n+1} - u_n)^2 - (u_n - u_{n-1})^2\right], \tag{9.2}$$

where $\omega_n = \sqrt{\frac{\beta}{m}}$

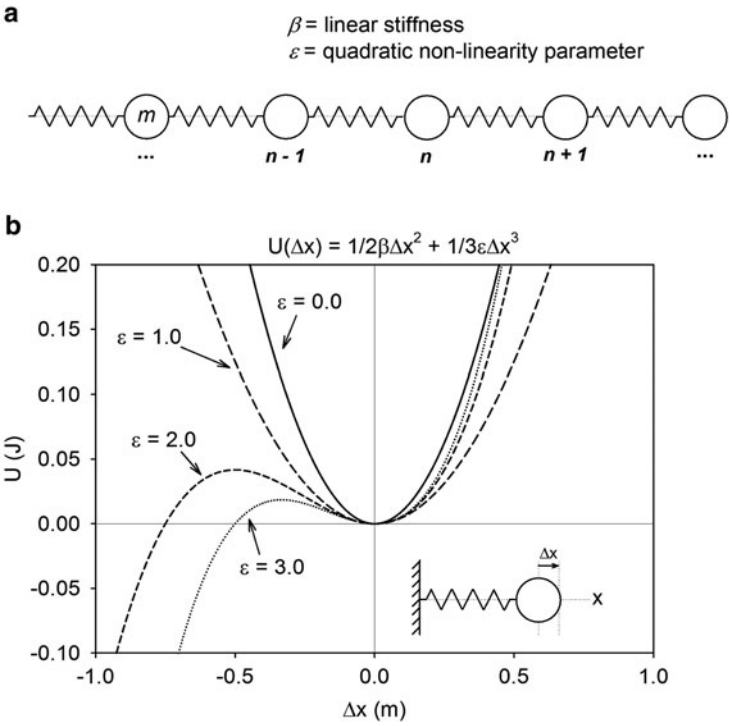

Fig. 9.1 (**a**) Schematic representation of 1D crystal with linear stiffness β and quadratic nonlinearity parameter ε. (**b**) The potential energy function describing the 1D crystal

The dependent variable in (9.2), $u_n(\tau)$, is expressed as an asymptotic expansion at multiple time scales:

$$u_n(\tau) = u_n^{(0)}(\tau) + \varepsilon u_n^{(1)}(\tau) + \varepsilon^2 u_n^{(2)}(\tau) + \text{higher order terms} \tag{9.3}$$

With this (9.2) is decomposed into equations for each order of expansion of ε, namely, the following set of equations:

$$\mathrm{O}(\varepsilon^0) : \frac{\partial^2 u_n^{(0)}}{\partial {\tau_0}^2} = {\omega_n}^2 \left(u_{n+1}^{(0)} - 2u_n^{(0)} + u_{n-1}^{(0)} \right)$$

$$O(\varepsilon^1) : \frac{\partial^2 u_n^{(1)}}{\partial {\tau_0}^2} + 2\frac{\partial^2 u_n^{(0)}}{\partial \tau_0 \partial \tau_1} = {\omega_n}^2 \left(u_{n+1}^{(1)} - 2u_n^{(1)} + u_{n-1}^{(1)} \right) + \frac{1}{m}\left[u_{n+1}^{(0)} u_{n+1}^{(0)} - 2u_{n+1}^{(0)} u_n^{(0)} + 2u_{n-1}^{(0)} u_n^{(0)} - u_{n-1}^{(0)} u_{n-1}^{(0)} \right]$$

$$O(\varepsilon^2): \frac{\partial^2 u_n^{(2)}}{\partial \tau_0{}^2} + 2\frac{\partial^2 u_n^{(1)}}{\partial \tau_0 \partial \tau_1} + 2\frac{\partial^2 u_n^{(0)}}{\partial \tau_0 \partial \tau_2} + \frac{\partial^2 u_n^{(0)}}{\partial \tau_1{}^2} = {\omega_n}^2\left(u_{n+1}^{(2)} - 2u_n^{(2)} + u_{n-1}^{(2)}\right) + \frac{2}{m}\left[u_{n+1}^{(1)}u_{n+1}^{(0)} - u_{n+1}^{(1)}u_n^{(0)} - u_{n+1}^{(0)}u_n^{(1)} + u_{n-1}^{(1)}u_n^{(0)} + u_{n-1}^{(0)}u_n^{(1)} - u_{n-1}^{(1)}u_{n-1}^{(0)}\right]$$

9.2.1.1 Self-Interaction

We first address the self-interaction of a vibrational mode, that is, the effect of the lattice deformation on itself. To solve the ε^0-equation, a general solution of the following form is proposed:

$$u_{n,G}^{(0)}(\tau_0, \tau_1, \tau_2) = A_0(\tau_1, \tau_2)\, \mathrm{e}^{\mathrm{i}kna}\mathrm{e}^{-\mathrm{i}\omega_0\tau_0} + \bar{A}_0(\tau_1, \tau_2)\, \mathrm{e}^{-\mathrm{i}kna}\mathrm{e}^{\mathrm{i}\omega_0\tau_0}, \tag{9.4}$$

where

$$A_0(\tau_1, \tau_2) = \alpha(\tau_1, \tau_2)\, \mathrm{e}^{-\mathrm{i}\varphi(\tau_1, \tau_2)}$$

$$\bar{A}_0(\tau_1, \tau_2) = \alpha(\tau_1, \tau_2)\, \mathrm{e}^{\mathrm{i}\varphi(\tau_1, \tau_2)}$$

$A_0(\tau_1,\tau_2)$ is a complex quantity that permits slow time evolution of amplitude and phase and $\alpha(\tau_1, \tau_2)$ and $\varphi(\tau_1, \tau_2)$ are real-valued functions. Inserting (9.4) into the ε^0-order equation yields the well-known dispersion relationship for the harmonic system (9.5):

$${\omega_0}^2 = {\omega_n}^2\left(2 - \mathrm{e}^{\mathrm{i}ka} - \mathrm{e}^{-\mathrm{i}ka}\right) = \frac{\beta}{m}\left[2 - 2\cos(ka)\right] \tag{9.5}$$

Equation (9.4) is now utilized in the ε^1-order equation to resolve the general solution for $u_n^{(1)}$. The ε^1-order equation is written as follows:

$$\frac{\partial^2 u_n^{(1)}}{\partial \tau_0{}^2} + {\omega_n}^2\left(2u_n^{(1)} - u_{n+1}^{(1)} - u_{n-1}^{(1)}\right) = 2i\omega_0\left[\frac{\partial A_0}{\partial \tau_1}\mathrm{e}^{\mathrm{i}kna}\mathrm{e}^{-\mathrm{i}\omega_0\tau_0} - \frac{\partial \bar{A}_0}{\partial \tau_1}\mathrm{e}^{-\mathrm{i}kna}\mathrm{e}^{\mathrm{i}\omega_0\tau_0}\right] + \frac{1}{m}\left[\left(\mathrm{e}^{\mathrm{i}2ka} - 2\mathrm{e}^{\mathrm{i}ka} + 2\mathrm{e}^{-\mathrm{i}ka} - \mathrm{e}^{-\mathrm{i}2ka}\right)\left(A_0A_0\mathrm{e}^{\mathrm{i}2kna}\mathrm{e}^{-\mathrm{i}2\omega_0\tau_0} - \bar{A}_0\bar{A}_0\mathrm{e}^{-\mathrm{i}2kna}\mathrm{e}^{\mathrm{i}2\omega_0\tau_0}\right)\right]$$

It is assumed that the solution to the homogeneous equation of the ε^1-order equation takes similar form to the general solution of the ε^0-order equation. Under this assumption, terms on the RHS of the ε^1-order equation with functional form $\mathrm{e}^{\mathrm{i}\omega_0\tau_0}$ or $\mathrm{e}^{-\mathrm{i}\omega_0\tau_0}$ contribute to secular behavior. These terms are eliminated by setting them equal to zero. Accordingly, A_0 and $\bar{A}_0$ are considered to be independent functions of τ_1. This modifies the form of the general solution to the ε^0-equation:

$$u_{n,G}^{(0)}(\tau_0,\tau_2) = A_0(\tau_2)\,\mathrm{e}^{\mathrm{i}kna}\mathrm{e}^{-\mathrm{i}\omega_0\tau_0} + \bar{A}_0(\tau_2)\,\mathrm{e}^{-\mathrm{i}kna}\mathrm{e}^{\mathrm{i}\omega_0\tau_0}, \tag{9.6}$$

where

$$A_0(\tau_2) = \alpha(\tau_2)\mathrm{e}^{-\mathrm{i}\varphi(\tau_2)}$$

$$\bar{A}_0(\tau_2) = \alpha(\tau_2)\,\mathrm{e}^{\mathrm{i}\varphi(\tau_2)}$$

The homogeneous solution to the ε^1-order equation takes the following form:

$$u_{n,H}^{(1)}(\tau_0,\tau_2) = B_0(\tau_2)\mathrm{e}^{\mathrm{i}kna}\mathrm{e}^{-\mathrm{i}\omega_0\tau_0} + \bar{B}_0(\tau_2)\mathrm{e}^{-\mathrm{i}kna}\mathrm{e}^{\mathrm{i}\omega_0\tau_0} \tag{9.7}$$

The particular solution to the ε^1-order equation is of the form:

$$u_{n,P}^{(1)}(\tau_0,\tau_2) = C_0(\tau_2)\mathrm{e}^{\mathrm{i}2kna}\mathrm{e}^{-\mathrm{i}2\omega_0\tau_0} + \bar{C}_0(\tau_2)\mathrm{e}^{-\mathrm{i}2kna}\mathrm{e}^{\mathrm{i}2\omega_0\tau_0} \tag{9.8}$$

Inserting (9.8) into the ε^1-order equation and relating like terms reveals relationships for the exponential pre-factors $C_0(\tau_2)$ and $\bar{C}_0(\tau_2)$. Equation (9.8) becomes

$$u_{n,P}^{(1)}(\tau_0,\tau_2) = \frac{2i(\sin(2ka) - 2\sin(ka))}{\beta((2-2\cos) - 4(2-2\cos(ka)))}\left[{A_0}^2\mathrm{e}^{\mathrm{i}2kna}\mathrm{e}^{-\mathrm{i}2\omega_0\tau_0} - {\bar{A}_0}^2\mathrm{e}^{-\mathrm{i}2kna}\mathrm{e}^{\mathrm{i}2\omega_0\tau_0}\right].$$

The general solution to the ε^1-order equation is a sum of the homogeneous ($u_{n,H}^{(1)}$) and particular solutions ($u_{n,P}^{(1)}$):

$$\begin{aligned} u_{n,G}^{(1)}(\tau_0,\tau_2) = {} & B_0\mathrm{e}^{\mathrm{i}kna}\mathrm{e}^{-\mathrm{i}\omega_0\tau_0} + \bar{B}_0\,\mathrm{e}^{-\mathrm{i}kna}\mathrm{e}^{\mathrm{i}\omega_0\tau_0} \\ & + \frac{2i(\sin(2ka) - 2\sin(ka))}{\beta((2-2\cos(2ka)) - 4(2-2\cos(ka)))} \\ & \times \left[A_0A_0\mathrm{e}^{\mathrm{i}2kna}\mathrm{e}^{-\mathrm{i}2\omega_0\tau_0} - \bar{A}_0\bar{A}_0\mathrm{e}^{-\mathrm{i}2kna}\mathrm{e}^{\mathrm{i}2\omega_0\tau_0}\right] \end{aligned}$$

The values for B_0 and $\bar{B}_0$ are found from initial conditions. With the general solutions to the ε^0-equation and the ε^1-equation, the ε^2-order equation is developed. Inserting $u_{n,G}^{(0)}$ and $u_{n,G}^{(1)}$ into the ε^2-order equation, utilizing the expressions for $A_0(\tau_2)$ and $\bar{A}_0(\tau_2)$, and noting that $u_n^{(0)}$ and $u_n^{(1)}$ are independent functions of τ_1, the ε^2-order equation is written as

$$\frac{\partial^2 u_n^{(2)}}{\partial {\tau_0}^2} + {\omega_n}^2\left(2u_n^{(2)} - u_{n+1}^{(2)} - u_{n-1}^{(2)}\right) =$$

$$
\begin{aligned}
&\mathrm{e}^{\mathrm{i}kna}\mathrm{e}^{-\mathrm{i}\omega_0\tau_0}\left(2\omega_0\alpha\frac{\partial\varphi}{\partial\tau_2}\mathrm{e}^{-\mathrm{i}\varphi}+2i\omega_0\mathrm{e}^{-\mathrm{i}\varphi}\frac{\partial\alpha}{\partial\tau_2}\right)\\
&\quad+\mathrm{e}^{-\mathrm{i}kna}\mathrm{e}^{\mathrm{i}\omega_0\tau_0}\left(2\omega_0\alpha\frac{\partial\varphi}{\partial\tau_2}\mathrm{e}^{\mathrm{i}\varphi}-2i\omega_0\mathrm{e}^{\mathrm{i}\varphi}\frac{\partial\alpha}{\partial\tau_2}\right)\\
&\quad+\frac{2}{m}\left\{\left[\left(\mathrm{e}^{\mathrm{i}2ka}-2\mathrm{e}^{\mathrm{i}ka}+2\mathrm{e}^{-\mathrm{i}ka}-\mathrm{e}^{-\mathrm{i}2ka}\right)\left(A_0B_0\mathrm{e}^{\mathrm{i}2kna}\mathrm{e}^{-\mathrm{i}2\omega_0\tau_0}-\bar{A}_0\bar{B}_0\mathrm{e}^{-\mathrm{i}2kna}\mathrm{e}^{\mathrm{i}2\omega_0\tau_0}\right)\right]\right.\\
&\quad+\left[\left(\mathrm{e}^{\mathrm{i}3ka}-\mathrm{e}^{\mathrm{i}2ka}-\mathrm{e}^{\mathrm{i}ka}+\mathrm{e}^{-\mathrm{i}ka}+\mathrm{e}^{-\mathrm{i}2ka}-\mathrm{e}^{-\mathrm{i}3ka}\right)\right.\\
&\quad\left.\times\left(A_0C_0\mathrm{e}^{\mathrm{i}3kna}\mathrm{e}^{-\mathrm{i}3\omega_0\tau_0}-\bar{A}_0\bar{C}_0\mathrm{e}^{-\mathrm{i}3kna}\mathrm{e}^{\mathrm{i}3\omega_0\tau_0}\right)\right]\\
&\quad\left.+\left[\left(\mathrm{e}^{\mathrm{i}2ka}-2\mathrm{e}^{\mathrm{i}ka}+2\mathrm{e}^{-\mathrm{i}ka}-\mathrm{e}^{-\mathrm{i}2ka}\right)\left(A_0\bar{C}_0\mathrm{e}^{-\mathrm{i}kna}\mathrm{e}^{\mathrm{i}\omega_0\tau_0}-\bar{A}_0C_0\mathrm{e}^{\mathrm{i}kna}\mathrm{e}^{-\mathrm{i}\omega_0\tau_0}\right)\right]\right\}
\end{aligned}
$$

The homogeneous solution to the ε^2-order equation is similar in form to the general solution of the ε^0-equation and the homogeneous solution of the ε^1-equation. Accordingly, terms on the RHS of the ε^2-order equation with functional form $\mathrm{e}^{\mathrm{i}\omega_0\tau_0}$ or $\mathrm{e}^{-\mathrm{i}\omega_0\tau_0}$ contribute to secular behavior and must be eliminated. Setting exponential pre-factors equal to zero yields the following relationships for $\alpha(\tau_2)$ and $\varphi(\tau_2)$:

$$\alpha(\tau_2)=\alpha_0 \tag{9.9}$$

$$\varphi(\tau_2)=-\frac{\alpha^2}{\omega_0\beta m}\cdot\frac{4(\sin(2ka)-2\sin(ka))^2}{(2-2\cos(2ka))-4(2-2\cos(ka))}\tau_2+\varphi_0, \tag{9.10}$$

where α_0 and φ_0 are constants determined from initial plane wave conditions. The general solution to the ε^0-equation [(9.6)] is considered again with (9.9) and (9.10) utilized in expressions for A_0 and $\bar{A}_0$. Here, the constant φ_0 can be set equal to zero without loss of generality.

$$
\begin{aligned}
u_{n,G}^{(0)}(\tau_0,\tau_2)=\alpha_0\mathrm{e}^{\mathrm{i}\left(kna-\left(\omega_0-\varepsilon^2\frac{\alpha^2}{\omega_0\beta m}\cdot\frac{4(\sin(2ka)-2\sin(ka))^2}{(2-2\cos(2ka))-4(2-2\cos(ka))}\right)\tau_0\right)}\\
+\alpha_0\mathrm{e}^{-\mathrm{i}\left(kna-\left(\omega_0-\varepsilon^2\frac{\alpha^2}{\omega_0\beta m}\cdot\frac{4(\sin(2ka)-2\sin(ka))^2}{(2-2\cos(2ka))-4(2-2\cos(ka))}\right)\tau_0\right)}
\end{aligned}
$$

This result shows that the 0th order term in the asymptotic expansion of u_n shows the harmonic dispersion curve to be shifted by a quantity that has quadratic dependence on the strength of the nonlinearity parameter ε.

9.2.1.2 Three-Wave Interactions

Here we consider the interaction between three waves with different wave vectors and frequencies. The analysis begins with the equation of motion [(9.1)] from the single-wave dispersion analysis. The displacement of the nth mass is represented by a superposition of wave modes each with a unique, time and wave vector-dependent amplitude factor [(9.11)]:

$$u_n(t) = \sum_k A(k,t)\mathrm{e}^{\mathrm{i}kna} \tag{9.11}$$

Here we use a discrete summation over the wave numbers instead of an integral over a continuum of wave vectors. This is done to help the reader to conceptualize the interactions between specific phonons and to facilitate the comparison with the MD models presented subsequently. Indeed, MD simulations are limited to finite size systems for which the phonon modes do not form a continuum but a discrete set of possible wave vectors. Inserting (9.11) into the equation of motion for the 1D monoatomic crystal yields a modified equation of motion [(9.12)].

$$= -4\beta\sum_k A(k,t)\mathrm{e}^{\mathrm{i}kna}\sin^2\left(\frac{ka}{2}\right) + \varepsilon\left[\sum_{k'}\sum_{k''} A(k',t)A(k'',t)\mathrm{e}^{i(k'+k'')na} f(k',k'')\right], \tag{9.12}$$

where $f(k',k'') = -8i\sin\left(\frac{k'a}{2}\right)\sin\left(\frac{k''a}{2}\right)\sin\left(\frac{(k'+k'')a}{2}\right)$. Equation (9.12) is multiplied by $\mathrm{e}^{-\mathrm{i}k^*na}$ and a summation over all n masses is imposed. This procedure selects the mode k^*as reference wave vector. With $\omega_n^2 = \frac{4\beta}{m}$, (9.12) becomes

$$\frac{\mathrm{d}^2A(k^*,t)}{\mathrm{d}t^2} + \omega_n^2\sin^2\left(\frac{k^*a}{2}\right)A(k^*,t) = \frac{\varepsilon}{m}\sum_{k'}\sum_{k''} A(k',t)A(k'',t)f(k',k'')\delta_{k'+k'',k^*} \tag{9.13}$$

$\delta_{k'+k'',k^*}$ imposes the wave vector conservation rule $k^* = k' + k'' + mG$ where m is an integer and G is a reciprocal lattice vector of the periodic structure. We do not label G in the delta function for the sake of simplicity of the notation. For $m = 0$, one has the so-called normal three phonon scattering process. The case of $m \neq 0$ corresponds to umklapp processes where $k' + k''$ is located outside the first Brillouin zone. In (9.13), the variable τ is introduced, where $\tau = \omega_n t$. Single time variables (τ) are replaced by a collection of variables $\tau = (\tau_0, \tau_1, \tau_2)$ whereby: $\tau_0 = \tau$, $\tau_1 = \varepsilon\tau$, $\tau_2 = \varepsilon^2\tau$. Additionally, $A(k^*, \tau)$ is replaced by an asymptotic expansion whereby:

$$A(k^*,\tau) = A_0(k^*,\tau) + \varepsilon A_1(k^*,\tau) + \varepsilon^2 A_2(k^*,\tau)$$
$$A(k^*,\tau_0,\tau_1,\tau_2) = A_0(k^*,\tau_0,\tau_1,\tau_2) + \varepsilon A_1(k^*,\tau_0,\tau_1,\tau_2) + \varepsilon^2 A_2(k^*,\tau_0,\tau_1,\tau_2)$$

With these considerations, (9.13) is separated into expressions at order ε^0, ε^1, and ε^2:

$O(\varepsilon^0)$:

$$\frac{\partial^2 A_0(k^*,\tau)}{\partial\tau_0^2} + \sin^2\left(\frac{k^*a}{2}\right)A_0(k^*,\tau) = 0$$

$O(\varepsilon^1)$:

$$\frac{\partial^2 A_1(k^*,\tau)}{\partial \tau_0^2} + 2\frac{\partial^2 A_0(k^*,\tau)}{\partial \tau_1 \partial \tau_0} + \sin^2\left(\frac{k^* a}{2}\right) A_1(k^*,\tau)$$
$$= \frac{1}{m\omega_n^2} \sum_{k'} \sum_{k''} f(k',k'') \delta_{k'+k'',k^*} [A_0(k',\tau) A_0(k'',\tau)]$$

$O(\varepsilon^2)$:

$$\frac{\partial^2 A_2(k^*,\tau)}{\partial \tau_0^2} + 2\frac{\partial^2 A_1(k^*,\tau)}{\partial \tau_1 \partial \tau_0} + 2\frac{\partial^2 A_0(k^*,\tau)}{\partial \tau_2 \partial \tau_0} + \frac{\partial^2 A_0(k^*,\tau)}{\partial \tau_1^2} + \sin^2\left(\frac{k^* a}{2}\right) A_2(k^*,\tau)$$
$$= \frac{1}{m\omega_n^2} \sum_{k'} \sum_{k''} f(k',k'') \delta_{k'+k'',k^*} [A_0(k',\tau) A_1(k'',\tau) + A_1(k',\tau) A_0(k'',\tau)]$$

To solve the ε^0-equation, a general solution of the following form is proposed:

$$A_0(k^*,\tau_0,\tau_1,\tau_2) = a_0(k^*,\tau_1,\tau_2) e^{i\omega_0^* \tau_0} + \bar{a}_0(k^*,\tau_1,\tau_2) e^{-i\omega_0^* \tau_0} \tag{9.14}$$

Inserting (9.14) into the ε^0-equation offers the expected relationship between ω_0^* and k^*:$\omega_0^{*2} = \sin^2\left(\frac{k^* a}{2}\right)$. Inserting (9.14) into the ε^1-equation offers an expression to solve for $A_1(k^*,\tau)$. After rearranging and utilizing the following definitions

$$A_0(k',\tau_0,\tau_1,\tau_2) = a_0(k',\tau_1,\tau_2) e^{i\omega'_0 \tau_0} + \bar{a}_0(k',\tau_1,\tau_2) e^{-i\omega'_0 \tau_0}$$

$$A_0(k'',\tau_0,\tau_1,\tau_2) = a_0(k'',\tau_1,\tau_2) e^{i\omega''_0 \tau_0} + \bar{a}_0(k'',\tau_1,\tau_2) e^{-i\omega''_0 \tau_0}$$

the ε^1-equation becomes

$$\frac{\partial^2 A_1(k^*,\tau)}{\partial \tau_0^2} + \omega_0^{*2} A_1(k^*,\tau) = -2i\omega_0^* \left[\frac{\partial a_0^*}{\partial \tau_1} e^{i\omega_0^* \tau_0} - \frac{\partial \bar{a}_0^*}{\partial \tau_1} e^{-i\omega_0^* \tau_0}\right]$$
$$+ \frac{1}{m\omega_n^2} \sum_{k'} \sum_{k''} f(k',k'') \delta_{k'+k'',k^*} [a'_0 a''_0 e^{i(\omega'_0+\omega''_0)\tau_0} + a'_0 \bar{a}''_0 e^{i(\omega'_0-\omega''_0)\tau_0}$$
$$+ \bar{a}'_0 a''_0 e^{-i(\omega'_0-\omega''_0)\tau_0} + \bar{a}'_0 \bar{a}''_0 e^{-i(\omega'_0+\omega''_0)\tau_0}]$$

where terms like $a_0^*, a'_0, a'' \ldots$ etc. are compact representations for $a_0(k^*,\tau_1,\tau_2)$, $a_0(k',\tau_1,\tau_2), a_0(k'',\tau_1,\tau_2) \ldots$ etc. A homogeneous solution to the ε^1-equation is proposed:

$$A_{1,H}(k^*,\tau_0,\tau_2) = a_1(k^*,\tau_2) e^{i\omega_0^* \tau_0} + \bar{a}_1(k^*,\tau_2) e^{-i\omega_0^* \tau_0} = a_1^* e^{i\omega_0^* \tau_0} + \bar{a}^*{}_1 e^{-i\omega_0^* \tau_0} \tag{9.15}$$

The forcing terms on the right hand side (RHS) of the ε^1-equation with functional form $e^{i\omega_0^* \tau_0}$ or $e^{-i\omega_0^* \tau_0}$ contribute to secular behavior. These terms must be eliminated such that the final representation of $A(k^*, \tau)$ is well behaved (e.g.contains no terms that temporally grow without bound). These terms are set to zero by making a_0 and $\bar{a}_0$

functions of k^* and τ_2 only. With this stipulation, an appropriate form of the particular solution to the ε^1-equation is:

$$A_{1,P}(k^*,\tau) = \frac{1}{m\omega_n^2}\sum_{k'}\sum_{k''} f(k',k'')\delta_{k'+k'',k^*} \times \left[b_1 e^{i(\omega'_0+\omega''_0)\tau_0} + \bar{b}_1 e^{-i(\omega'_0+\omega''_0)\tau_0} + c_1 e^{i(\omega'_0-\omega''_0)\tau_0} + \bar{c}_1 e^{-i(\omega'_0-\omega''_0)\tau_0}\right] \tag{9.16}$$

The exponential pre-factors $b_1, \bar{b}_1, c_1, \bar{c}_1$ have dependency on $k', k'', \tau_2, \omega_0^*, \omega'_0, \omega''_0$. Substituting (9.16) into the ε^1-equation and relating like terms reveals the exponential pre-factors: $b_1, \bar{b}_1, c_1, \bar{c}_1$

$$b_1 = \frac{a_0(k',\tau_2)a_0(k'',\tau_2)}{\omega_0^{*2} - (\omega'_0+\omega''_0)^2};\ \bar{b}_1 = \frac{\bar{a}_0(k',\tau_2)\bar{a}_0(k'',\tau_2)}{\omega_0^{*2} - (\omega'_0+\omega''_0)^2}$$

$$c_1 = \frac{a_0(k',\tau_2)\bar{a}_0(k'',\tau_2)}{\omega_0^{*2} - (\omega'_0-\omega''_0)^2};\ \bar{c}_1 = \frac{\bar{a}_0(k',\tau_2)a_0(k'',\tau_2)}{\omega_0^{*2} - (\omega'_0-\omega''_0)^2}$$

In the long wavelength limit, angular frequency has nearly linear dependence on wave vector. In considering the stipulated wave vector relationship inside the double summation in (9.16), $(k' + k'' = k^*)$, it is conceivable that $\omega_0(k') + \omega_0(k'') = \omega_0(k^*)$ or $\omega_0(k') - \omega_0(k'') = \omega_0(k^*)$. In this instance, the denominator terms in the expressions for $b_1, \bar{b}_1, c_1, \bar{c}_1$ will go to zero. To avoid this complication, following the procedure stipulated by Khoo et al. [17], a small imaginary part φ is introduced in the denominator. At the final result of the calculation a limit will be taken as $\varphi \to 0$. The general solution to the ε^1-equation is a sum of the homogeneous and particular solutions:

$$A_1(k^*,\tau_0,\tau_2) = a_1^* e^{i\omega_0^*\tau_0} + \bar{a}_1^* e^{-i\omega_0^*\tau_0} + \frac{1}{m\omega_n^2}\sum_{k'}\sum_{k''} f(k',k'')\delta_{k'+k'',k^*} \times \left[\frac{a'_0 a''_0}{g_1^*} e^{i(\omega'_0+\omega''_0)\tau_0} + \frac{\bar{a}'_0\bar{a}''_0}{g_1^*} e^{-i(\omega'_0+\omega''_0)\tau_0} + \frac{a'_0\bar{a}''_0}{g_2^*} e^{i(\omega'_0-\omega''_0)\tau_0} + \frac{\bar{a}'_0 a''_0}{g_2^*} e^{-i(\omega'_0-\omega''_0)\tau_0}\right], \tag{9.17}$$

where $g_1^* = \omega_0^{*2} - (\omega'_0+\omega''_0)^2 + i\varphi; g_2^* = \omega_0^{*2} - (\omega'_0-\omega''_0)^2 + i\varphi$

The ε^2-equation is reduced to the following expressions because $A_0(k^*,\tau)$ and $A_1(k^*,\tau)$ are independent of τ_1:

$$\frac{\partial^2 A_2(k^*,\tau_0,\tau_1,\tau_2)}{\partial\tau_0^2}+\omega_0^{*2}A_2(k^*,\tau_0,\tau_1,\tau_2)$$
$$=-2i\omega_0^*\frac{\partial a_0(k^*,\tau_2)}{\partial\tau_2}\mathrm{e}^{\mathrm{i}\omega_0^*\tau_0}+2i\omega_0^*\frac{\partial\bar{a}_0(k^*,\tau_2)}{\partial\tau_2}\mathrm{e}^{-\mathrm{i}\omega_0^*\tau_0}$$
$$+\frac{1}{m\omega_n^2}\sum_{k'}\sum_{k''}f(k',k'')\delta_{k'+k'',k^*}[A_0(k',\tau_0,\tau_2)A_1(k'',\tau_0,\tau_2)$$
$$+A_1(k',\tau_0,\tau_2)A_0(k'',\tau_0,\tau_2)]$$

As before, the solution to the homogeneous equation of the ε^2-equation is of the form:

$$A_{2,H}(k^*,\tau_0,\tau_2)=a_2(k^*,\tau_2)\mathrm{e}^{\mathrm{i}\omega_0^*\tau_0}+\bar{a}_2(k^*,\tau_2)\mathrm{e}^{-\mathrm{i}\omega_0^*\tau_0}$$

Terms on the RHS of the ε^2-equation with functional form $\mathrm{e}^{\mathrm{i}\omega_0^*\tau_0}$ or $\mathrm{e}^{-\mathrm{i}\omega_0^*\tau_0}$ contribute to secular behavior. Using equations (9.14) and (9.17) to develop the RHS of the ε^2-equation gives (9.18):

$$\frac{\partial^2 A_2(k^*,\tau_0,\tau_1,\tau_2)}{\partial\tau_0^2}+\omega_0^{*2}A_2(k^*,\tau_0,\tau_1,\tau_2)$$
$$=-2i\omega_0^*\frac{\partial a_0(k^*,\tau_2)}{\partial\tau_2}\mathrm{e}^{\mathrm{i}\omega_0^*\tau_0}+2i\omega_0^*\frac{\partial\bar{a}_0(k^*,\tau_2)}{\partial\tau_2}\mathrm{e}^{-\mathrm{i}\omega_0^*\tau_0}$$
$$+\frac{1}{m{\omega_n}^2}\sum_{k'}\sum_{k''}f(k',k'')\delta_{k'+k'',k^*}\left(a'_0a''_1\mathrm{e}^{\mathrm{i}(\omega'_0+\omega''_0)\tau_0}+a'_0\bar{a}''_1\mathrm{e}^{\mathrm{i}\left(\omega'_0-\omega''_0\right)\tau_0}\right.$$
$$\left.+\bar{a}'_0a''_1\mathrm{e}^{-\mathrm{i}\left(\omega'_0-\omega''_0\right)\tau_0}+\bar{a}'_0\bar{a}''_1\mathrm{e}^{-\mathrm{i}(\omega'_0+\omega''_0)\tau_0}\right)$$
$$+\frac{1}{m{\omega_n}^2}\sum_{k'}\sum_{k''}f(k',k'')\delta_{k'+k'',k^*}\left(a''_0a'_1\mathrm{e}^{\mathrm{i}(\omega''_0+\omega'_0)\tau_0}+a''_0\bar{a}'_1\mathrm{e}^{\mathrm{i}(\omega''_0-\omega'_0)\tau_0}\right.$$
$$\left.+\bar{a}''_0a'_1\mathrm{e}^{-\mathrm{i}(\omega''_0-\omega'_0)\tau_0}+\bar{a}''_0\bar{a}'_1\mathrm{e}^{-\mathrm{i}(\omega''_0+\omega'_0)\tau_0}\right)$$
$$+\frac{1}{m\omega_n^2}\sum_{k'}\sum_{k''}f(k',k'')\delta_{k'+k'',k^*}\left\{\left[\frac{1}{m\omega_n^2}\sum_{k_1}\sum_{k_2}f(k_1,k_2)\delta_{k_1+k_2,k''}\right.\right.$$
$$\left[\frac{a'_0a_0^{(1)}a_0^{(2)}}{g''_1}\mathrm{e}^{\mathrm{i}(\omega_0^{(1)}+\omega_0^{(2)}+\omega'_0)\tau_0}+\frac{a'_0\,\bar{a}_0^{(1)}\,\bar{a}_0^{(2)}}{g''_1}\mathrm{e}^{-\mathrm{i}(\omega_0^{(1)}+\omega_0^{(2)}-\omega'_0)\tau_0}\right.$$
$$+\frac{a'_0a_0^{(1)}\bar{a}_0^{(2)}}{g''_2}\mathrm{e}^{\mathrm{i}(\omega_0^{(1)}-\omega_0^{(2)}+\omega'_0)\tau_0}+\frac{a'_0\,\bar{a}_0^{(1)}\,a_0^{(2)}}{g''_2}\mathrm{e}^{-\mathrm{i}(\omega_0^{(1)}-\omega_0^{(2)}-\omega'_0)\tau_0}$$
$$\frac{\bar{a}'_0a_0^{(1)}a_0^{(2)}}{g''_1}\mathrm{e}^{\mathrm{i}(\omega_0^{(1)}+\omega_0^{(2)}-\omega'_0)\tau_0}+\frac{\bar{a}'_0\,\bar{a}_0^{(1)}\,\bar{a}_0^{(2)}}{g''_1}\mathrm{e}^{-\mathrm{i}(\omega_0^{(1)}+\omega_0^{(2)}+\omega'_0)\tau_0}$$
$$\left.\left.+\frac{\bar{a}'_0\,a_0^{(1)}\bar{a}_0^{(2)}}{g''_2}\mathrm{e}^{\mathrm{i}(\omega_0^{(1)}-\omega_0^{(2)}-\omega'_0)\tau_0}+\frac{\bar{a}'_0\bar{a}_0^{(1)}\,a_0^{(2)}}{g''_2}\mathrm{e}^{-\mathrm{i}(\omega_0^{(1)}-\omega_0^{(2)}+\omega'_0)\tau_0}\right]\right]$$

$$
\begin{aligned}
&+\left[\frac{1}{m\omega_n^2}\sum_{k_1}\sum_{k_2} f(k_1,k_2)\delta_{k_1+k_2,k'}\right.\\
&\times\left[\frac{a_0'' a_0^{(1)} a_0^{(2)}}{g'_1}\mathrm{e}^{\mathrm{i}(\omega_0^{(1)}+\omega_0^{(2)}+\omega''_0)\tau_0}+\frac{a_0'' \bar{a}_0^{(1)} \bar{a}_0^{(2)}}{g'_1}\mathrm{e}^{-\mathrm{i}(\omega_0^{(1)}+\omega_0^{(2)}-\omega''_0)\tau_0}\right.\\
&+\frac{a_0'' a_0^{(1)} \bar{a}_0^{(2)}}{g'_2}\mathrm{e}^{\mathrm{i}(\omega_0^{(1)}-\omega_0^{(2)}+\omega''_0)\tau_0}+\frac{a_0'' \bar{a}_0^{(1)} a_0^{(2)}}{g'_2}\mathrm{e}^{-\mathrm{i}(\omega_0^{(1)}-\omega_0^{(2)}-\omega''_0)\tau_0}\\
&+\frac{\bar{a}_0'' a_0^{(1)} a_0^{(2)}}{g'_1}\mathrm{e}^{\mathrm{i}(\omega_0^{(1)}+\omega_0^{(2)}-\omega''_0)\tau_0}+\frac{\bar{a}_0'' \bar{a}_0^{(1)} \bar{a}_0^{(2)}}{g'_1}\mathrm{e}^{-\mathrm{i}(\omega_0^{(1)}+\omega_0^{(2)}+\omega''_0)\tau_0}\\
&\left.\left.\left.+\frac{\bar{a}_0'' a_0^{(1)} \bar{a}_0^{(2)}}{g'_2}\mathrm{e}^{\mathrm{i}(\omega_0^{(1)}-\omega_0^{(2)}-\omega''_0)\tau_0}+\frac{\bar{a}_0'' \bar{a}_0^{(1)} a_0^{(2)}}{g'_2}\mathrm{e}^{-\mathrm{i}(\omega_0^{(1)}-\omega_0^{(2)}+\omega''_0)\tau_0}\right]\right]\right\}
\end{aligned}
\tag{9.18}
$$

There is notable similarity between the terms on the RHS of the ε^1-equation that was solved to yield (9.17) and the third and fourth terms on the RHS of (9.18). These terms are treated with the same procedure as that used for the ε^1-equation. Accordingly, they will not contribute to secular terms.

The objective is to identify terms in the ε^2-equation with $\mathrm{e}^{\mathrm{i}\omega_0^*\tau_0}$ or $\mathrm{e}^{-\mathrm{i}\omega_0^*\tau_0}$ dependency. This will be done by systematically evaluating all wave vector pairs $\{k_1, k_2\}$ that satisfy the wave vector constraints stipulated by (9.18). Specifically,

$$
\begin{aligned}
\delta_{k'+k'',k^*}\delta_{k_1+k_2,k''} &\rightarrow k'+k_1+k_2=k^*\\
\delta_{k'+k'',k^*}\delta_{k_1+k_2,k'} &\rightarrow k''+k_1+k_2=k^*.
\end{aligned}
$$

If a certain pair of wave vectors satisfies the above-mentioned wave vector constraints, then an analysis will be carried through to see if these wave vectors give rise to terms with $\mathrm{e}^{\mathrm{i}\omega_0^*\tau_0}$ or $\mathrm{e}^{-\mathrm{i}\omega_0^*\tau_0}$ dependence. As before, terms with $\mathrm{e}^{\mathrm{i}\omega_0^*\tau_0}$ or $\mathrm{e}^{-\mathrm{i}\omega_0^*\tau_0}$ dependence will be removed.

In (9.18), inside the summation over k', k'', there are two summations over k_1, k_2. For the first summation over k_1, k_2 , two conditions must be met: (1) $k'+k''=k^*$ and (2) $k_1+k_2=k''$.

The only possible combinations for k_1, k_2 that give wave vector relationships that are compatible with $\delta_{k'+k'',k^*}$ are shown as Condition A and Condition B:

$$\text{Condition A}: k_1=-k', k_2=k^* \text{and} -k'+k^*=k''$$

$$\text{Condition B}: k_1=k^*, k_2=-k\prime, \text{and}\, k^*-k'=k''$$

Now that wave vector constraints are satisfied, an analysis is carried out to see if any terms with $\mathrm{e}^{\mathrm{i}\omega_0^*\tau_0}$ or $\mathrm{e}^{-\mathrm{i}\omega_0^*\tau_0}$ dependence arise in the first summation over k_1, k_2.

The following frequency relationships are present in the first summation over k_1, k_2 in (9.18):

(i). $\omega_0^{(1)} + \omega_0^{(2)} + \omega_0'$
(ii). $\omega_0^{(1)} + \omega_0^{(2)} - \omega_0'$
(iii). $\omega_0^{(1)} - \omega_0^{(2)} + \omega_0'$
(iv). $\omega_0^{(1)} - \omega_0^{(2)} - \omega\prime_0$

Applying Condition A to these frequency relationships show two relationships that offer terms with $e^{i\omega_0^* \tau_0}$ or $e^{-i\omega_0^* \tau_0}$ dependence:

$$\text{Condition A} : k_1 = -k' \rightarrow \omega_0^{(1)} = \omega_0' \,\text{and}\, k_2 = k^* \rightarrow \omega_0^{(2)} = \omega_0^*$$

Applying Condition A to frequency relationships leads to:

(i). $\omega_0^{(1)} + \omega_0^{(2)} + \omega_0' \rightarrow \omega_0' + \omega_0^* + \omega_0' = \omega_0^* + 2\omega_0'$
(ii). $\omega_0^{(1)} + \omega_0^{(2)} - \omega_0' \rightarrow \omega_0' + \omega_0^* - \omega_0' = \omega_0^*$
(iii). $\omega_0^{(1)} - \omega_0^{(2)} + \omega_0' \rightarrow \omega_0' - \omega_0^* + \omega_0' = -\omega_0^* + 2\omega_0'$
(iv). $\omega_0^{(1)} - \omega_0^{(2)} - \omega_0' \rightarrow \omega_0' - \omega_0^* - \omega_0' = -\omega_0^*$

As a result, with Condition A, the following terms in the first summation over k_1, k_2 contribute to secular terms:

$$\frac{a_0' \bar{a}_0^{(1)} \bar{a}_0^{(2)}}{g''_1} e^{-i(\omega_0^{(1)} + \omega_0^{(2)} - \omega'_0)\tau_0} = \frac{a_0' \bar{a}_0' \bar{a}_0^*}{g''_1} e^{-i(\omega'_0 + \omega_0^* - \omega'_0)\tau_0} = \frac{a_0' \bar{a}_0' \bar{a}_0^*}{g''_1} e^{-i(\omega_0^*)\tau_0}$$

$$\frac{\bar{a}_0' a_0^{(1)} a_0^{(2)}}{g''_1} e^{i(\omega_0^{(1)} + \omega_0^{(2)} - \omega'_0)\tau_0} = \frac{\bar{a}_0' a_0' a_0^*}{g''_1} e^{i(\omega'_0 + \omega_0^* - \omega'_0)\tau_0} = \frac{\bar{a}_0' a_0' a_0^*}{g''_1} e^{i(\omega_0^*)\tau_0}$$

$$\frac{a_0' \bar{a}_0^{(1)} a_0^{(2)}}{g''_2} e^{-i(\omega_0^{(1)} - \omega_0^{(2)} - \omega'_0)\tau_0} = \frac{a_0' \bar{a}_0' a_0^*}{g''_2} e^{-i(\omega'_0 - \omega_0^* - \omega'_0)\tau_0} = \frac{a_0' \bar{a}_0^{(1)} a_0^{(2)}}{g''_2} e^{i(\omega_0^*)\tau_0}$$

$$\frac{\bar{a}_0' a_0^{(1)} \bar{a}_0^{(2)}}{g''_2} e^{i(\omega_0^{(1)} - \omega_0^{(2)} - \omega'_0)\tau_0} = \frac{\bar{a}_0' a_0' \bar{a}_0^*}{g''_2} e^{i(\omega'_0 - \omega_0^* - \omega'_0)\tau_0} = \frac{\bar{a}_0' a_0^{(1)} \bar{a}_0^{(2)}}{g''_2} e^{-i(\omega_0^*)\tau_0}$$

Applying Condition B to these frequency relationships show two different relationships that offer terms with $e^{i\omega_0^* \tau_0}$ or $e^{-i\omega_0^* \tau_0}$ dependence:

$$\text{Condition B} : k_1 = k^* \rightarrow \omega_0^{(1)} = \omega_0^*, k_2 = -k' \rightarrow \omega_0^{(2)} = \omega_0'$$

Applying Condition B to frequency relationships leads to:

(i). $\omega_0^{(1)} + \omega_0^{(2)} + \omega_0' \rightarrow \omega_0^* + \omega_0' + \omega_0' = \omega_0^* + 2\omega_0'$
(ii). $\omega_0^{(1)} + \omega_0^{(2)} - \omega_0' \rightarrow \omega_0^* + \omega_0' - \omega_0' = \omega_0^*$
(iii). $\omega_0^{(1)} - \omega_0^{(2)} + \omega_0' \rightarrow \omega_0^* - \omega_0' + \omega_0' = \omega_0^*$
(iv). $\omega_0^{(1)} - \omega_0^{(2)} - \omega_0' \rightarrow \omega_0^* - \omega_0' - \omega_0' = \omega_0^* - 2\omega_0'$

As a result, with Condition B, the following terms in the first summation over k_1, k_2 contribute to secular terms:

$$\frac{a_0' \bar{a}_0^{(1)} \bar{a}_0^{(2)}}{g''_1} e^{-i(\omega_0^{(1)}+\omega_0^{(2)}-\omega'_0)\tau_0} = \frac{a_0' \bar{a}_0^{*} \bar{a}_0'}{g''_1} e^{-i(\omega_0^{*}+\omega'_0-\omega'_0)\tau_0} = \frac{a_0' \bar{a}_0^{*} \bar{a}_0'}{g''_1} e^{-i(\omega_0^{*})\tau_0}$$

$$\frac{\bar{a}_0' a_0^{(1)} a_0^{(2)}}{g''_1} e^{i(\omega_0^{(1)}+\omega_0^{(2)}-\omega'_0)\tau_0} = \frac{\bar{a}_0' a_0^{*} a_0'}{g''_1} e^{i(\omega_0^{*}+\omega'_0-\omega'_0)\tau_0} = \frac{\bar{a}_0' a_0^{*} a_0'}{g''_1} e^{i(\omega_0^{*})\tau_0}$$

$$\frac{a_0' a_0^{(1)} \bar{a}_0^{(2)}}{g''_2} e^{i(\omega_0^{(1)}-\omega_0^{(2)}+\omega'_0)\tau_0} = \frac{a_0' a_0^{*} \bar{a}_0'}{g''_2} e^{i(\omega_0^{*}-\omega'_0+\omega'_0)\tau_0} = \frac{a_0' a_0^{*} \bar{a}_0'}{g''_2} e^{i(\omega_0^{*})\tau_0}$$

$$\frac{\bar{a}_0' \bar{a}_0^{(1)} a_0^{(2)}}{g''_2} e^{-i(\omega_0^{(1)}-\omega_0^{(2)}+\omega'_0)\tau_0} = \frac{\bar{a}_0' \bar{a}_0^{*} a_0'}{g''_2} e^{-i(\omega_0^{*}-\omega'_0+\omega'_0)\tau_0} = \frac{\bar{a}_0' \bar{a}_0^{*} a_0'}{g''_2} e^{-i(\omega_0^{*})\tau_0}$$

For the second summation over k_1, k_2 , two conditions must be met:
(1) $k' + k'' = k^*$
(2) $k_1 + k_2 = k'$

The only possible combinations for k_1, k_2 that give wave vector relationships that are compatible with $\delta_{k'+k'',k^*}$ are shown as Condition C and Condition D:

$$\text{Condition C} : k_1 = -k'', k_2 = k*, \text{and} - k'' + k* = k'$$

$$\text{Condition D} : k_1 = k^*, k_2 = -k'', \text{ and } k^* - k'' = k$$

Now that wave vector constraints are satisfied, an analysis is carried out to see if any terms with $e^{i\omega_0^* \tau_0}$ or $e^{-i\omega_0^* \tau_0}$ dependency arise in the second summation over k_1, k_2. The following frequency relationships are present in the second summation over k_1, k_2 in (9.18):
(v). $\omega_0^{(1)} + \omega_0^{(2)} + \omega_0''$
(vi). $\omega_0^{(1)} + \omega_0^{(2)} - \omega_0''$
(vii). $\omega_0^{(1)} - \omega_0^{(2)} + \omega_0''$
(viii). $\omega_0^{(1)} - \omega_0^{(2)} - \omega_0''$

Applying Condition C to these frequency relationships show two relationships that offer terms with $e^{i\omega_0^* \tau_0}$ or $e^{-i\omega_0^* \tau_0}$ dependence:

$$\text{Condition C} : k_1 = -k'' \rightarrow \omega_0^{(1)} = \omega_0'' \quad \text{and} \quad k_2 = k^* \rightarrow \omega_0^{(2)} = \omega_0^*$$

Applying Condition C to frequency relationships leads to
(v). $\omega_0^{(1)} + \omega_0^{(2)} + \omega_0'' \rightarrow \omega_0'' + \omega_0^* + \omega_0'' = \omega_0^* + 2\omega_0''$
(vi). $\omega_0^{(1)} + \omega_0^{(2)} - \omega_0'' \rightarrow \omega_0'' + \omega_0^* - \omega_0'' = \omega_0^*$
(vii). $\omega_0^{(1)} - \omega_0^{(2)} + \omega_0'' \rightarrow \omega_0'' - \omega_0^* + \omega_0'' = -\omega_0^* + 2\omega_0''$
(viii). $\omega_0^{(1)} - \omega_0^{(2)} - \omega_0'' \rightarrow \omega_0'' - \omega_0^* - \omega_0'' = -\omega_0^*$

As a result, with Condition C, the following terms in the second summation over k_1, k_2 contribute to secular terms:

$$\frac{a_0'' \bar{a}_0^{(1)} \bar{a}_0^{(2)}}{g'_1} e^{-i(\omega_0^{(1)}+\omega_0^{(2)}-\omega''_0)\tau_0} = \frac{a_0'' \bar{a}_0'' \bar{a}_0^*}{g'_1} e^{-i(\omega''_0+\omega_0^*-\omega''_0)\tau_0} = \frac{a_0'' \bar{a}_0'' \bar{a}_0^*}{g'_1} e^{-i(\omega_0^*)\tau_0}$$

$$\frac{\bar{a}_0'' a_0^{(1)} a_0^{(2)}}{g'_1} e^{i(\omega_0^{(1)}+\omega_0^{(2)}-\omega''_0)\tau_0} = \frac{\bar{a}_0'' a_0'' a_0^*}{g'_1} e^{i(\omega''_0+\omega_0^*-\omega''_0)\tau_0} = \frac{\bar{a}_0'' a_0^* a_0''}{g'_1} e^{i(\omega_0^*)\tau_0}$$

$$\frac{a_0'' \bar{a}_0^{(1)} a_0^{(2)}}{g'_2} e^{-i(\omega_0^{(1)}-\omega_0^{(2)}-\omega''_0)\tau_0} = \frac{a_0'' \bar{a}_0'' a_0^*}{g'_2} e^{-i(\omega''_0-\omega_0^*-\omega''_0)\tau_0} = \frac{a_0'' \bar{a}_0'' a_0^*}{g'_2} e^{i(\omega_0^*)\tau_0}$$

$$\frac{\bar{a}_0'' a_0^{(1)} \bar{a}_0^{(2)}}{g'_2} e^{i(\omega_0^{(1)}-\omega_0^{(2)}-\omega''_0)\tau_0} = \frac{\bar{a}_0'' a_0'' \bar{a}_0^*}{g'_2} e^{i(\omega''_0-\omega_0^*-\omega''_0)\tau_0} = \frac{\bar{a}_0'' a_0'' \bar{a}_0^*}{g'_2} e^{-i(\omega_0^*)\tau_0}$$

Applying Condition D to these frequency relationships show two different relationships that offer terms with $e^{i\omega_0^*\tau_0}$ or $e^{-i\omega_0^*\tau_0}$ dependence:

$$\text{Condition D} : k_1 = k^* \rightarrow \omega_0^{(1)} = \omega_0^* \text{and } k_2 = -k'' \rightarrow \omega_0^{(2)} = \omega_0''$$

Applying Condition D to frequency relationships leads to
(v). $\omega_0^{(1)} + \omega_0^{(2)} + \omega_0'' \rightarrow \omega_0^* + \omega_0'' + \omega_0'' = \omega_0^* + 2\omega_0''$
(vi). $\omega_0^{(1)} + \omega_0^{(2)} - \omega_0'' \rightarrow \omega_0^* + \omega_0'' - \omega_0'' = \omega_0^*$
(vii). $\omega_0^{(1)} - \omega_0^{(2)} + \omega_0'' \rightarrow \omega_0^* - \omega_0'' + \omega_0'' = \omega_0^*$
(viii). $\omega_0^{(1)} - \omega_0^{(2)} - \omega_0'' \rightarrow \omega_0^* - \omega_0'' - \omega_0'' = \omega_0^* - 2\omega_0''$

As a result, with Condition D, the following terms in the second summation over k_1, k_2 contribute to secular terms:

$$\frac{a_0'' \bar{a}_0^{(1)} \bar{a}_0^{(2)}}{g'_1} e^{-i(\omega_0^{(1)}+\omega_0^{(2)}-\omega''_0)\tau_0} = \frac{a_0'' \bar{a}_0^* \bar{a}_0''}{g'_1} e^{-i(\omega_0^*+\omega''_0-\omega''_0)\tau_0} = \frac{a_0'' \bar{a}_0^* \bar{a}_0''}{g'_1} e^{-i(\omega_0^*)\tau_0}$$

$$\frac{\bar{a}_0'' a_0^{(1)} a_0^{(2)}}{g'_1} e^{i(\omega_0^{(1)}+\omega_0^{(2)}-\omega''_0)\tau_0} = \frac{\bar{a}_0'' a_0^* a_0''}{g'_1} e^{i(\omega_0^*+\omega''_0-\omega''_0)\tau_0} = \frac{\bar{a}_0'' a_0^* a_0''}{g'_1} e^{i(\omega_0^*)\tau_0}$$

$$\frac{a_0'' a_0^{(1)} \bar{a}_0^{(2)}}{g'_2} e^{i(\omega_0^{(1)}-\omega_0^{(2)}+\omega''_0)\tau_0} = \frac{a_0'' a_0^* \bar{a}_0''}{g'_2} e^{i(\omega_0^*-\omega''_0+\omega''_0)\tau_0} = \frac{a_0'' a_0^* \bar{a}_0''}{g'_2} e^{i(\omega_0^*)\tau_0}$$

$$\frac{\bar{a}_0'' \bar{a}_0^{(1)} a_0^{(2)}}{g'_2} e^{-i(\omega_0^{(1)}-\omega_0^{(2)}+\omega''_0)\tau_0} = \frac{\bar{a}_0'' \bar{a}_0^* a_0''}{g'_2} e^{-i(\omega_0^*-\omega''_0+\omega''_0)\tau_0} = \frac{\bar{a}_0'' \bar{a}_0^* a_0''}{g'_2} e^{-i(\omega_0^*)\tau_0}$$

In assuming that terms $[a_0(k'), \bar{a}_0(k'), a_0(-k'), \bar{a}_0(-k'), \ldots, \text{etc.}]$in (9.18) behave as follows:

$$a_0(k', \tau_2) = a_0(k', 0)\mathrm{e}^{\mathrm{i}\beta(k')\tau_2}$$

$$\bar{a}_0(k', \tau_2) = \bar{a}_0(k', 0)\mathrm{e}^{-\mathrm{i}\beta(k')\tau_2}$$

$$a_0(-k', \tau_2) = a_0(-k', 0)\mathrm{e}^{\mathrm{i}\beta(-k')\tau_2}$$

$$\bar{a}_0(-k', \tau_2) = \bar{a}_0(-k', 0)\mathrm{e}^{-\mathrm{i}\beta(-k')\tau_2}$$

$$\vdots$$

etc.

Additionally,

$$a_0(k', 0) = a_0(-k', 0)$$

$$\bar{a}_0(k', 0) = \bar{a}_0(-k', 0)$$

$$\beta(k') = \beta(-k')$$

Equation (9.18) can be rewritten in the form of (9.19):

$$\begin{aligned}
&\frac{\partial^2 A_2(k^*, \tau_0, \tau_1, \tau_2)}{\partial \tau_0^2} + \omega_0^{*2} A_2(k^*, \tau_0, \tau_1, \tau_2) \\
&= \left\{ -2i\omega_0^* \frac{\partial a_0(k^*, \tau_2)}{\partial \tau_2} + a_0(k^*, 0)\mathrm{e}^{\mathrm{i}\beta(k^*)\tau_2} \left(\frac{1}{m\omega_n^2}\right)^2 \sum_{k'} \sum_{k''} f(k', k'')\delta_{k'+k'', k^*} \right. \\
&\quad \times \left[2f(-k', k^*)\delta_{-k'+k^*, k''} a_0(k', 0)\bar{a}_0(k', 0) \left[\frac{1}{{g''}_1} + \frac{1}{{g''}_2} \right] \right. \\
&\quad \left. \left. + 2f(-k'', k^*)\delta_{-k''+k^*, k'} a_0(k'', 0)\bar{a}_0(k'', 0) \left[\frac{1}{{g'}_1} + \frac{1}{{g'}_2} \right] \right] \right\} \mathrm{e}^{\mathrm{i}\omega_0^*\tau_0} \\
&\quad + \left\{ 2i\omega_0^* \frac{\partial \bar{a}_0(k^*, \tau_2)}{\partial \tau_2} + \bar{a}_0(k^*, 0)\mathrm{e}^{-\mathrm{i}\beta(k^*)\tau_2} \left(\frac{1}{m\omega_n^2}\right)^2 \right. \\
&\quad \times \sum_{k'} \sum_{k''} f(k', k'')\delta_{k'+k'', k^*} \left[2f(-k', k^*)\delta_{-k'+k^*, k''} a_0(k', 0)\bar{a}_0(k', 0) \right. \\
&\quad \times \left[\frac{1}{{g''}_1} + \frac{1}{{g''}_2} \right] + 2f(-k'', k^*)\delta_{-k''+k^*, k'} a_0(k'', 0)\bar{a}_0(k'', 0) \left[\frac{1}{{g'}_1} + \frac{1}{{g'}_2} \right] \left. \left. \right] \right\} \mathrm{e}^{-\mathrm{i}\omega_0^*\tau_0} \\
&\quad + \text{other terms which will not give } \mathrm{e}^{\mathrm{i}\omega_0^*\tau_0} \text{ or } \mathrm{e}^{-\mathrm{i}\omega_0^*\tau_0} \text{ dependence}
\end{aligned} \tag{9.19}$$

The terms in front of $\mathrm{e}^{\mathrm{i}\omega_0^*\tau_0}$ and $\mathrm{e}^{-\mathrm{i}\omega_0^*\tau_0}$ are set to zero. This is shown by equations (9.20) and (9.21):

$$a_0(k^*,0)\mathrm{e}^{\mathrm{i}\beta(k^*)\tau_2}\left(\frac{1}{m\omega_n^2}\right)^2\sum_{k'}\sum_{k''} f(k',k'')\delta_{k'+k'',k^*}\Bigg[2f(-k',k^*)\delta_{-k'+k^*,k''}a_0(k',0)\bar{a}_0(k',0) \times\left[\frac{1}{g''_1}+\frac{1}{g''_2}\right]+2f(-k'',k^*)\delta_{-k''+k^*,k'}a_0(k'',0)\bar{a}_0(k'',0)\left[\frac{1}{g'_1}+\frac{1}{g'_2}\right]\Bigg] = -2\omega_0^*\beta(k^*)a_0(k^*,0)\mathrm{e}^{\mathrm{i}\beta(k^*)\tau_2} \tag{9.20}$$

$$\bar{a}_0(k^*,0)\mathrm{e}^{-\mathrm{i}\beta(k^*)\tau_2}\left(\frac{1}{m\omega_n^2}\right)^2\sum_{k'}\sum_{k''} f(k',k'')\delta_{k'+k'',k^*}\Big[2f(-k',k^*)\delta_{-k'+k^*,k''}a_0(k',0)\bar{a}_0(k',0) \times\left[\frac{1}{g''_1}+\frac{1}{g''_2}\right]+2f(-k'',k^*)\delta_{-k''+k^*,k'}a_0(k'',0)\bar{a}_0(k'',0)\left[\frac{1}{g'_1}+\frac{1}{g'_2}\right]\Big] = -2\omega_0^*\beta(k^*)\bar{a}_0(k^*,0)\mathrm{e}^{-\mathrm{i}\beta(k^*)\tau_2} \tag{9.21}$$

From (9.20) and (9.21), the same expression for β^* results [(9.22)]:

$$\beta(k^*) = -\frac{1}{2\omega_0^*}\left(\frac{1}{m\omega_n^2}\right)^2\sum_{k'}\sum_{k''} f(k',k'')\delta_{k'+k'',k^*}\Big[2f(-k',k^*)\delta_{-k'+k^*,k''}a_0(k',0)\bar{a}_0(k',0) \times\left[\frac{1}{g''_1}+\frac{1}{g''_2}\right]+2f(-k'',k^*)\delta_{-k''+k^*,k'}a_0(k'',0)\bar{a}_0(k'',0)\left[\frac{1}{g'_1}+\frac{1}{g'_2}\right]\Big] \tag{9.22}$$

Recall that φ appears in the terms containing g''_1, g''_2, g'_1, g'_2 The limit of (9.22) is taken as $\varphi \to 0$. The following definition is utilized [17]:

$$\lim_{\theta\to 0}\frac{1}{(x\pm i\theta)} = \left(\frac{1}{x}\right)_{\mathrm{pp}} \mp i\pi\delta(x)$$

where pp denotes principle part. The real and imaginary parts of (9.22) are shown as (9.23) and (9.24), respectively.

$$\mathrm{Re}(\beta^*) = \Delta_{k^*} = \frac{-64}{\omega_0^*}\left(\frac{1}{m\omega_n^2}\right)^2 \sum_{k'}\sum_{k''} \sin^2\left(\frac{k'a}{2}\right)\sin^2\left(\frac{k''a}{2}\right)\sin^2\left(\frac{k^*a}{2}\right)$$
$$\left\{ a_0'\bar{a}'_0 \left[\left(\frac{1}{\omega_0''^2 - \left(\omega_0^* + \omega_0'\right)^2}\right)_{\mathrm{pp}} + \left(\frac{1}{\omega_0''^2 - \left(\omega_0^* - \omega_0'\right)^2}\right)_{\mathrm{pp}} \right] \right.$$
$$\left. + a_0''\bar{a}_0'' \left[\left(\frac{1}{\omega_0'^2 - \left(\omega_0^* + \omega_0''\right)^2}\right)_{\mathrm{pp}} + \left(\frac{1}{\omega_0'^2 - \left(\omega_0^* - \omega_0''\right)^2}\right)_{\mathrm{pp}} \right] \right\} \tag{9.23}$$

$$\mathrm{Im}(\beta^*) = \Gamma_{k^*} = \frac{32\pi}{\omega_0^*}\left(\frac{1}{m\omega_n^2}\right)^2 \sum_{k'}\sum_{k''} \sin^2\left(\frac{k'a}{2}\right)\sin^2\left(\frac{k''a}{2}\right)\sin^2\left(\frac{k^*a}{2}\right)$$
$$\times \left\{ \delta\left(\omega_0^* + \omega_0' + \omega_0''\right)\left[\frac{a_0'\bar{a}_0'}{\omega_0''} + \frac{a_0''\bar{a}_0''}{\omega_0'}\right] - \delta\left(\omega_0^* + \omega_0' - \omega_0''\right) \right.$$
$$\times \left[\frac{a_0'\bar{a}_0'}{\omega_0''} - \frac{a_0''\bar{a}_0''}{\omega_0'}\right] + \delta\left(\omega_0^* - \omega_0' + \omega_0''\right)\left[\frac{a_0'\bar{a}_0'}{\omega_0''} - \frac{a_0''\bar{a}_0''}{\omega_0'}\right]$$
$$\left. - \delta\left(\omega_0^* - \omega_0' - \omega_0''\right)\left[\frac{a_0'\bar{a}'_0}{\omega_0''} + \frac{a_0''\bar{a}_0''}{\omega_0'}\right] \right\} \tag{9.24}$$

In the above expressions for the real and imaginary parts of β^*

$$a_0'\bar{a}_0' = a_0(k',0)\bar{a}_0(k',0)$$

$$a_0''\bar{a}'' = a_0(k'',0)\bar{a}_0(k'',0)$$

From here, the general solution to the ε^0-equation [(9.14)] is considered with the new found results for $a_0(k^*,\tau_2)$ and $\bar{a}_0(k^*,\tau_2)$:

$$a_0(k^*,\tau_2) = a_0(k^*,0)\mathrm{e}^{\mathrm{i}\beta(k^*)\tau_2}$$

$$\bar{a}_0(k^*,\tau_2) = \bar{a}_0(k^*,0)\mathrm{e}^{-\mathrm{i}\beta(k^*)\tau_2}$$

Equation (9.14) is written as follows:

$$A_0(k^*,\tau_0,\tau_2) = a_0(k^*,\tau_2)\mathrm{e}^{\mathrm{i}\omega_0^*\tau_0} + \bar{a}_0(k^*,\tau_2)\mathrm{e}^{-\mathrm{i}\omega_0^*\tau_0}$$

Utilizing the new found results for $a_0(k^*,\tau_2)$ and $\bar{a}_0(k^*,\tau_2)$, one arrives at the following expression:

$$A_0(k^*,\tau_0,\tau_2) = a_0(k^*,0)\mathrm{e}^{\mathrm{i}\left(\omega_0^*\tau_0+\beta(k^*)\tau_2\right)} + \bar{a}_0(k^*,0)\mathrm{e}^{-\mathrm{i}\left(\omega_0^*\tau_0+\beta(k^*)\tau_2\right)}$$

Writing the above expression strictly in terms of τ_0, where $\tau_2 = \varepsilon^2\tau_0$ gives the following representation for $A_0(k^*, \tau_0)$

$$A_0(k^*, \tau_0) = a_0(k^*, 0)\mathrm{e}^{\mathrm{i}\left(\omega_0^*\tau_0 + \varepsilon^2\beta(k^*)\tau_0\right)} + \bar{a}_0(k^*, 0)\mathrm{e}^{-\mathrm{i}\left(\omega_0^*\tau_0 + \varepsilon^2\beta(k^*)\tau_0\right)}$$

β^* is expressed in terms of its real and imaginary parts to yield the final representation for $A_0(k^*, \tau_0)$:

$$\beta(k^*) = \Delta_{k^*} + i\Gamma_{\mathrm{k}^*}$$

$$A_0(k^*, \tau_0) = a_0(k^*, 0)\mathrm{e}^{\mathrm{i}\left(\omega_0^*\tau_0 + \varepsilon^2(\Delta_{k^*} + i\Gamma_{\mathrm{k}^*})\tau_0\right)} + \bar{a}_0(k^*, 0)\mathrm{e}^{-\mathrm{i}\left(\omega_0^*\tau_0 + \varepsilon^2(\Delta_{k^*} + i\Gamma_{\mathrm{k}^*})\tau_0\right)}$$

$$\begin{aligned} A_0(k^*, \tau_0) = {} & a_0(k^*, 0)\mathrm{e}^{\mathrm{i}\left(\left(\omega_0^* + \varepsilon^2\Delta_{k^*}\right)\tau_0\right)}\mathrm{e}^{-\varepsilon^2\Gamma_{\mathrm{k}^*}\tau_0} \\ & + \bar{a}_0(k^*, 0)e^{-\mathrm{i}\left(\left(\omega_0^* + \varepsilon^2\Delta_{k^*}\right)\tau_0\right)}\mathrm{e}^{\varepsilon^2\Gamma_{\mathrm{k}^*}\tau_0} \end{aligned} \tag{9.25}$$

Three-wave interaction leads therefore to an additional frequency shift proportional to the square of the strength of the nonlinearity. Moreover, three-wave interaction leads to a damping of each wave, that is, a finite lifetime. This result is the classical mechanics equivalent of that reported within the framework of quantum mechanics [11–13, 17].

9.2.2 *Molecular Dynamics Simulation and Spectral Energy Density Approach*

In this section we shed additional light on the three phonon scattering processes in one-dimensional anharmonic crystals using the numerical method of MD. MD is a simulation technique for computing the thermodynamic as well as kinetic properties of a classical many-body system [18]. Classical MD methods consist of solving numerically Newton's equations of motion of a collection of N interacting particles or atoms. The most critical component of an MD simulation is the interatomic potential from which interatomic forces may be derived. The equation of motion of each individual atom is solved numerically in time to obtain the trajectories of the system, namely, the time evolution of the positions and momenta of every particle. In some systems the computational task of solving the equations of motion scales at best linearly with the number of particles, N, and more generally as N^2. Periodic boundary conditions (PBC) are often used to reduce the computational problem size. PBC consist of repeating periodically in all directions of space a "small" simulation cell. One allows interaction between the N atoms within the simulation cell and also between atoms inside the simulation cell and atoms in the periodically repeated "image" cells. Interactions are cut-off to less than half the minimum characteristic length of the simulation cell to avoid spurious

effects such as interaction of an atom with its own image. This method effectively reduces the effects that may be associated with surfaces associated with a finite size system. However, while trying to mimic the behavior of an infinite system, the simulated system still possesses the characteristics of a finite system. For instance, the finiteness of an MD system with PBC leads to a discretization of the phonon modes and a suppression of the modes with wavelength longer than the simulation cell length. This is easily seen by considering a 1D monoatomic system composed of N atoms interacting via a nearest neighbor harmonic (or anharmonic) potential. In this case, imposing PBC leads to atom N interacting with atom 1 thus forming a ring. Modes with wavelengths exceeding the length $L = Na$, where a is the interatomic spacing, are not compatible with the constraint of the ring geometry and cannot be supported by that structure. The finite number of modes will also impact the number of three phonon interactions that may take place in a finite simulation cell. The discrete phonon modes may not allow the requirement of frequency conservation. These points will be illustrated with numerical simulations of the 1D anharmonic monoatomic crystal.

For the present discussion, the equation of motion [(9.1)] for a toy system is integrated by MD techniques with PBC using the velocity Verlet algorithm under the microcanonical ensemble (constant energy)[18]. This scheme ensures that energy is conserved within 0.5%. Harmonic MD simulations of the 1D monoatomic crystal utilize $\beta = 1.0$ N/m and $\varepsilon = 0.0$ N/m^2 whereas anharmonic simulations utilize $\beta = 1.0$ N/m and $\varepsilon = [0.9{-}3.7]$ N/m^2. The 1D crystal consists of a chain of 1.0 kg masses spaced periodically 1.0 meter apart. These parameters can be easily scaled down to represent an atomic system. To initiate a simulation, every mass in the MD simulation cell is randomly displaced from its equilibrium position. The maximum value in which a mass can be displaced is constrained such that instabilities do not emerge in the potential energy function. MD simulations are run for 2^{21} time steps with a timestep of 0.01 s. For post-processing spectral energy density (SED) calculations, velocity data is collected for each mass in the simulation cell over the entire simulation time.

The SED method is a technique for predicting phonon dispersion relations and lifetimes from the atomic velocities of the particles in a crystal generated by classical MD [19]. The SED method offers a comprehensive description of phonon properties because individual phonon modes can be isolated for analysis and is computationally affordable for the systems that will be examined in this section. Formally, the expression for SED is written as follows:

$$\Phi(\vec{k},\omega) = \frac{1}{4\pi\tau_0 N}\sum_{\alpha}\sum_{b}^{B} m_b \left| \int_0^{\tau_0} \sum_{n_{x,y,z}}^{N} v_\alpha \begin{pmatrix} n_{x,y,z} \\ b \end{pmatrix}; t \times \mathrm{e}^{(\mathrm{i}\vec{k}\cdot\overrightarrow{r_0} - \mathrm{i}\omega t)} \mathrm{d}t \right|^2$$

where τ_0 represents the length of time over which velocity data is collected from a given MD simulation, N is the total number of unit cells represented in the MD simulation, and $v_\alpha \begin{pmatrix} n_{x,y,z} \\ b \end{pmatrix}; t$ represents the velocity of atom b (of mass m_b in unit cell $n_{x,y,z}$) in the α-direction. For a specified wave vector ($\vec{k}$), the spectrum relating

SED to frequency is found by adding the square of the absolute value of the Fourier transform of the discrete temporal signal $f(t) = \sum_{n_{x,y,z}}^{N_T} v_\alpha \left(\begin{matrix} n_{x,y,z} \\ b \end{matrix} ; t \right) \times e^{(i\vec{k}\cdot\overrightarrow{r_0})}$ for every $[\alpha, b]$ pair. A SED value represents the average kinetic energy per unit cell as a function of wave vector and frequency. A peak in the spectrum relating SED to frequency signifies a vibrational eigenmode for wave vector $(\vec{k})$. The shape of the frequency spread for eigenmode $(\vec{k})$ is represented with the Lorentzian function:

$$\Phi(\vec{k}, \omega) = \frac{I}{1 + [(\omega - \omega_c)/\gamma]^2}$$

where I is the peak magnitude, $\omega_c$is the frequency at the center of the peak, and γ is the half-width at half-maximum. The lifetime for phonon mode $(\vec{k})$ is defined as $\tau = 1/2\gamma$[19]. Nondegenerate wave vector modes are dependent on the size of the MD simulation cell and are written as follows: $k_i = 2\pi n_i / aN_i$, where a is the lattice constant, N_i is the total number of unit cells in the i-direction, and n_i is an integer ranging from $-N_i$+1 to N_i. The robust nature of the SED method is used to quantify specific phonon modes in several configurations of the 1D anharmonic crystal in the following subsections.

9.2.3 One-Dimensional Anharmonic Monoatomic Crystal

To begin with, the band structure generated by the SED method is shown for the 1D harmonic monoatomic crystal (Fig. 9.2). Figure 9.2 shows contours of constant SED over the wave vector-frequency plane.

There are 101 discrete, nondegenerate wave vectors resolved between the center of the irreducible Brillouin Zone and the zone edge at $k = \pi/a$. In the band structure, there is a nearly linear region that accounts for the propagative characteristics of long wavelength excitations in the 1D harmonic crystal. At larger wave vector values, a departure from the linear behavior is apparent and the phase velocity of propagative phonon modes is markedly different from the group velocity. This is similar to the expected dispersion behavior of the infinite monoatomic harmonic crystal. At the edge of the irreducible Brillouin zone, a SED-frequency plot is reported. A peak in the spectrum shows this vibrational mode contributing significantly to the average kinetic energy per unit cell. A Lorentzian function is fit to this peak and shows a finite value for half-width at half-maximum (γ) because the fast Fourier transform scheme used in the SED calculation involves a signal sampled over a finite time window. This value for half-width at half-maximum is subsequently used as a lower bound for the error on lifetime estimated with the SED method. This error amounts to one interval in the discrete frequency scale. The band structure of the harmonic system is highlighted in the long wavelength regime; Fig. 9.3 zooms in on a region of the dispersion curve near $k = \pi/10a$.

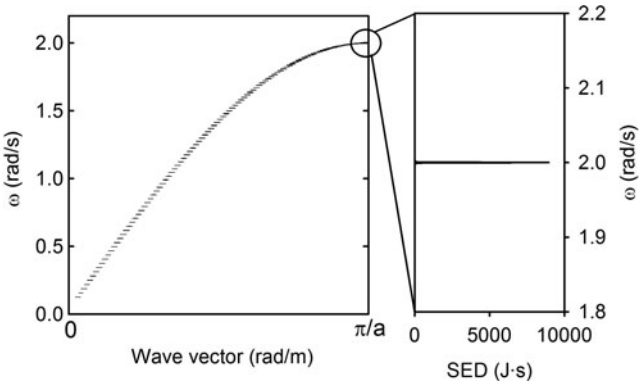

Fig. 9.2 (*Left*) Band Structure of 1D harmonic monoatomic crystal. (*Right*) SED-frequency plot showing wave vector mode $k = \pi/a$

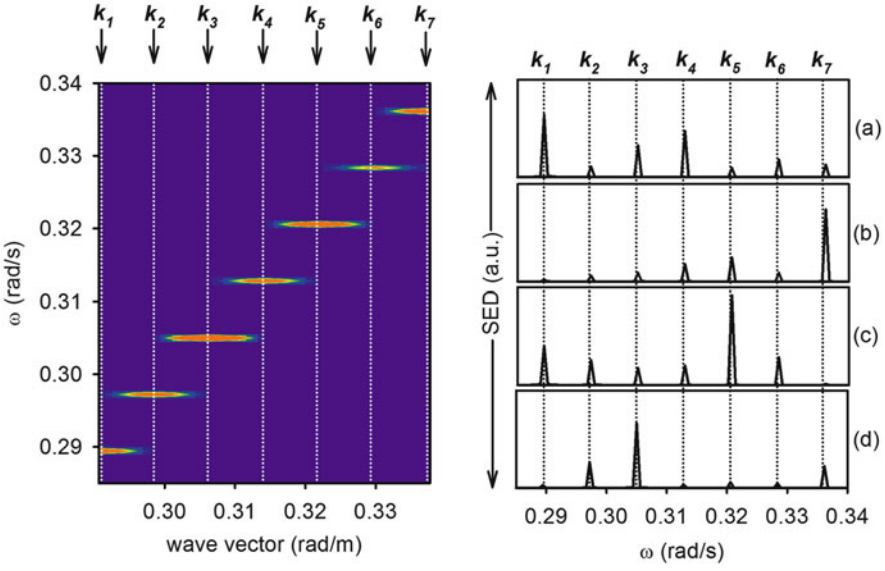

Fig. 9.3 (*Left*) Band Structure (constant SED contours) for 1D harmonic monoatomic crystal near $k = \pi/10a$. (*Right*) SED-frequency plots for four MD simulations differing in their initial random configurations

In Fig. 9.3 on the right hand side, four SED-frequency plots are shown (plots a–d). Each plot represents a different MD simulation of the 1D harmonic monoatomic crystal. Each MD simulation begins with a random starting configuration for atomic displacements in the 1D crystal. It is observable from these four plots that for a given wave vector, the SED takes on different values. This is due to the fact that for a harmonic crystal, energy contained within a particular mode cannot be passed to

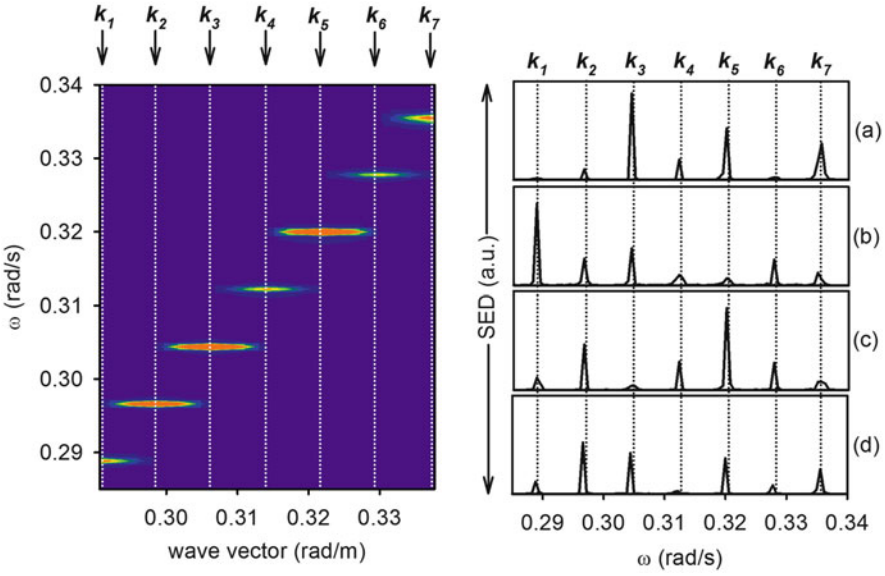

Fig. 9.4 (*Left*) Band Structure (constant SED contours) for 1D anharmonic monoatomic crystal near $k = \pi/10a$. (*Right*) SED-frequency plots for four MD simulations differing in their initial random configurations

other modes of vibration. This highlights the sensitivity of the vibrational modes of the harmonic crystal on the initial configuration. Consequently, to obtain a nonbiased band structure, multiple MD simulations must be run such that an average can be taken of the different SED values for each discrete, nondegenerate wave vector mode. An average of plots (a–d) is shown on the left hand side of Fig. 9.3 with the color of the contours signifying SED intensity. A Lorentzian function is fit to each of the peaks in the left hand figure and shows the same value for half-width at half-maximum as that calculated in Fig. 9.2. For comparison, the band structure of the 1D anharmonic monoatomic crystal near $k = \pi/10a$is shown in Fig. 9.4. Here the parameter characterizing the degree of anharmonicity in the 1D crystal is $\varepsilon = 3.0$ (see Fig. 9.1b).

Similar to Fig. 9.3, the four plots on the right hand side of Fig. 9.4 represent SED-frequency plots generated from four different MD simulations. The SED intensity for a given mode varies from simulation to simulation, which indicates that energy does not easily exchange between modes of vibration in the 1D anharmonic crystal. In contrast, though, there are some peaks in the SED-frequency spectra that show slightly larger values for half-width at half-maximum. However, it is critical that averages be taken for SED data extracted from several MD simulations such that an accurate quantification of phonon lifetime can be realized. The contour map on the left hand side of Fig. 9.4 represents an average over plots (a–d). Lorentzian functions are fit to the peaks in this figure. The half-width at half-maximum for all peaks is found to be comparable to the harmonic case. With a

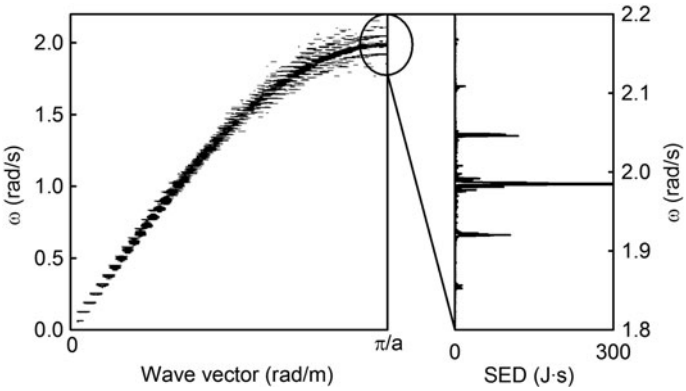

Fig. 9.5 (*Left*) Band Structure for 1D anharmonic monoatomic crystal. (*Right*) SED-frequency plot showing wave vector mode $k = \pi/a$. $\varepsilon = 3.0$ and initial random displacement does not exceed 10 % of a

random initial displacement of the masses of at most 10 % of the lattice spacing "a," the total energy of the anharmonic system is only 1.3 % higher than that of the harmonic system. Under this condition, the system can be considered to be weakly anharmonic and second order perturbation theory is applicable. In other words, the system studied here belongs to the category of weak coupling and is not expected to behave like the Fermi-Pasta-Ulam model where strong nonlinearity leads to persistent recurring vibrational modes[20]. Considering the final expression for $A_0(k^*, \tau_0)$ in Sect. 9.2.1 (9.25), which represents the 0th order term in the asymptotic expansion of $A(k^*, \tau)$ describing three-wave interactions, Γ_{k^*} (9.24) corresponds to a decay constant for mode k^*. Half-width at half-maximum calculations of peaks in SED-frequency spectra embody Γ_{k^*}. In the long wavelength regime, Γ_{k^*} is small because of squared sinusoidal terms inside the double summation over k' and k''. Accordingly, one should not expect large values for half-width at half-maximum in the long wavelength limit. The complete band structure for the 1D anharmonic monoatomic crystal is shown in Fig. 9.5. The band structure is generated from SED averages taken from four MD simulations.

In Fig. 9.5, it seems that each nondegenerate wave vector is associated with multiple eigenfrequencies due to the fact that multiple peaks appear in the SED. At the edge of the irreducible Brillouin zone, an intense central peak is seen along with multiple, less intense symmetrical satellite peaks. These satellite peaks emerge when the anharmonicity of the system is adequately sampled (i.e., large amplitudes of vibration). Equation (9.17) of Sect. 9.2.1 is utilized to explain the appearance of these satellite peaks. This equation represents the 1st order term in the asymptotic expansion of $A(k^*, \tau)$ describing three-wave interactions. Inside the double summation over (k', k'') in (9.17), conservation of wave vectors is imposed: $\delta_{k'+k'',k^*} \rightarrow k' + k'' = k^*$. If the mode of interest is $k^* = \pi/a$, then conservation of wave vector can be satisfied by adding nondegenerate wave vector pairs that yield k^*. With N = 400, nondegenerate wave vectors are limited to the following: $k_i = \frac{n_i}{400} \cdot \frac{2\pi}{a}$. If only wave

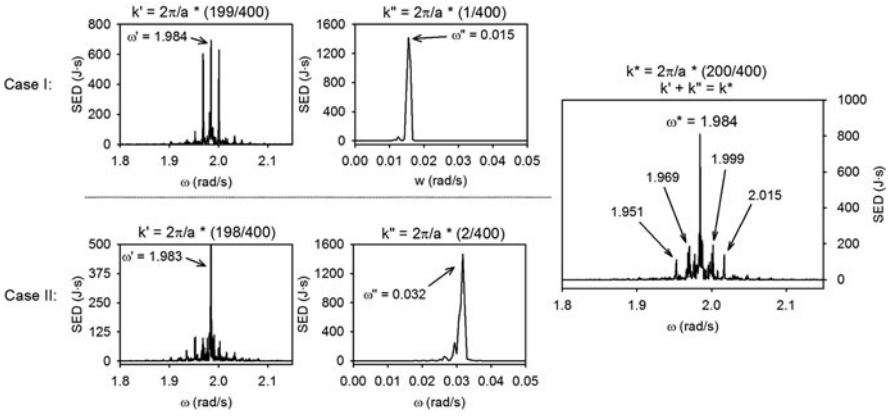

Fig. 9.6 (*Top, left*) SED-frequency plots for wave vector modes k and k corresponding to Case I. (*Bottom, left*) SED-frequency plots for wave vector modes k and k corresponding to Case II. (*Right*) SED-frequency plot corresponding to $k^* = \pi/a$. For Cases I and II, wave vectors k and k satisfy wave vector conservation for mode k^*. The frequencies of modes k and k add (or subtract) to yield near-resonance peaks near $\omega^*(k^*)$. Notice the frequency scale difference between short and long wavelength modes

vectors contained between the center of the irreducible Brillouin zone and the zone edge are considered, then n_i ranges from 0 to 200. As a first example, to satisfy wave vector conservation, consider two wave vectors: (1) the first nondegenerate wave vector before the zone edge at $(k = \pi/a)$ and (2) the first nondegenerate wave vector after the center of the irreducible Brillouin zone at $(k = 0)$. This pair of wave vectors is shown as Case I and satisfies wave vector conservation: (Case I) $k' = \frac{199}{400} \cdot \frac{2\pi}{a}$, $k'' = \frac{1}{400} \cdot \frac{2\pi}{a}$, $k^* = \frac{200}{400} \cdot \frac{2\pi}{a}$.

As a second example, consider (1) the second nondegenerate wave vector before the zone edge at $(k = \pi/a)$ and (2) the second nondegenerate wave vector after the center of the irreducible Brillouin zone at $(k = 0)$. This pair of wave vectors is defined as Case II and satisfies wave vector conservation: (Case II) $k' = \frac{198}{400} \cdot \frac{2\pi}{a}$, $k'' = \frac{2}{400} \cdot \frac{2\pi}{a}$, $k^* = \frac{200}{400} \cdot \frac{2\pi}{a}$. We note that both cases do not conserve frequency. In both cases, since the dispersion relationship for the 1D anharmonic monoatomic crystal is not strictly linear, the frequency of mode k' plus (or minus) the frequency of mode k'' will not exactly equal the frequency of mode k^*. Instead, the addition (or subtraction) of the frequencies associated with modes k' and k'' will be slightly greater than (or less than) the frequency of mode k^*. This forces the denominator of the pre-exponential factors in (9.17) to become small, thereby contributing to a large value of $A_1(k^*, \tau_0, \tau_2)$. The presence of nonzero $A_1(k^*, \tau_0, \tau_2)$ indicates that discrete, near-resonance modes are initiated for short wavelength phonons (k') interacting with long wavelength phonons (k''). On the left hand side of Fig. 9.6, we show nondegenerate wave vector modes k' and k'' corresponding to Case I (top) and Case II (bottom). On the right hand side, Fig. 9.6 shows the modes at $k^* = \pi/a$.

In this image the satellite peaks coincide with discrete, near-resonance modes. The central peak frequencies of modes k' and k'' add (or subtract) to yield satellite peaks to the central peak for $k^* = \pi/a$. The primary satellite peaks at 1.999 and 1.969 rad/s come from Case I. The secondary satellite peaks at 2.015 and 1.951 rad/s come from Case II. Tertiary, quaternary, and other higher order satellite peaks exist and are revealed if the scale on the right hand SED plot were adjusted. The magnitude of the satellite peaks depends upon the "distance" from the central peak at $k = \pi/a$ in accordance with their near resonant character. This distance depends upon the size of the MD simulation. For an MD simulation with $N = 100$ atoms, there are 51 discrete, nondegenerate wave vector modes available between the center of the irreducible Brillouin zone and the zone edge. For $N = 1{,}000$ atoms, there are 501 available modes. The resolution in wave vector-space is finer for larger MD systems as is the resolution in frequency-space. Higher frequency resolution results in smaller spacing between satellite peaks. This is shown in Fig. 9.7. As the number of atoms (N) increases, the satellite peaks congregate around the central peak and increase in relative amplitude. In the limit of an infinite system all satellite peaks merge into the central peak.

For a phonon mode to decay, wave vector and frequency conservation rules must be satisfied. For short wavelength phonon modes, these constraints are pathologically difficult to satisfy because the monoatomic dispersion curve is not linear. The central frequency peaks in Fig. 9.7 represent the resonance mode of wave vector $k = \pi/a$. The satellite peaks in Fig. 9.7 represent frequency-nonconserving near-resonance modes spawned from nonlinear wave interactions between short wavelength phonons and long wavelength phonons. The lifetime of phonon mode $k = \pi/a$ comes from fitting a Lorentzian function to the central peak. As Fig. 9.7 shows, the half-width at half-maximum for phonon mode $k = \pi/a$ is rather insensitive to the number of atoms in the MD simulation cell. It is found that the half-width at half-maximum for $k = \pi/a$ is the same order of magnitude as the error estimate found from the harmonic case in Fig. 9.2. As a result, lifetime of high-frequency phonon modes in the anharmonic monoatomic crystal is inherently long because wave vector and frequency conservation constraints cannot be satisfied.

In comparing the anharmonic band structure with the harmonic band structure at $(k = \pi/a)$, there is an obvious shift in frequency of the central peak. The perturbation analysis of the single-wave dispersion has shown that the anharmonic dispersion curve is frequency-shifted (with respect to the harmonic dispersion curve) by a quantity that has quadratic dependence on the strength of the nonlinearity parameter ε. Fig. 9.8 shows a plot mapping the frequency shift relative to the harmonic system for several values of ε for a MD simulation cell consisting of $N = 200$ atoms. In Fig. 9.8, three different curves are rendered. Each curve represents a different magnitude for the initial random displacement imposed upon the masses in the 1D crystal in terms of percentage lattice spacing. The magnitude of the initial displacement controls the amplitude of the phonon modes. For triangles, the maximum value a mass can be displaced is 10 % of the lattice spacing. For squares

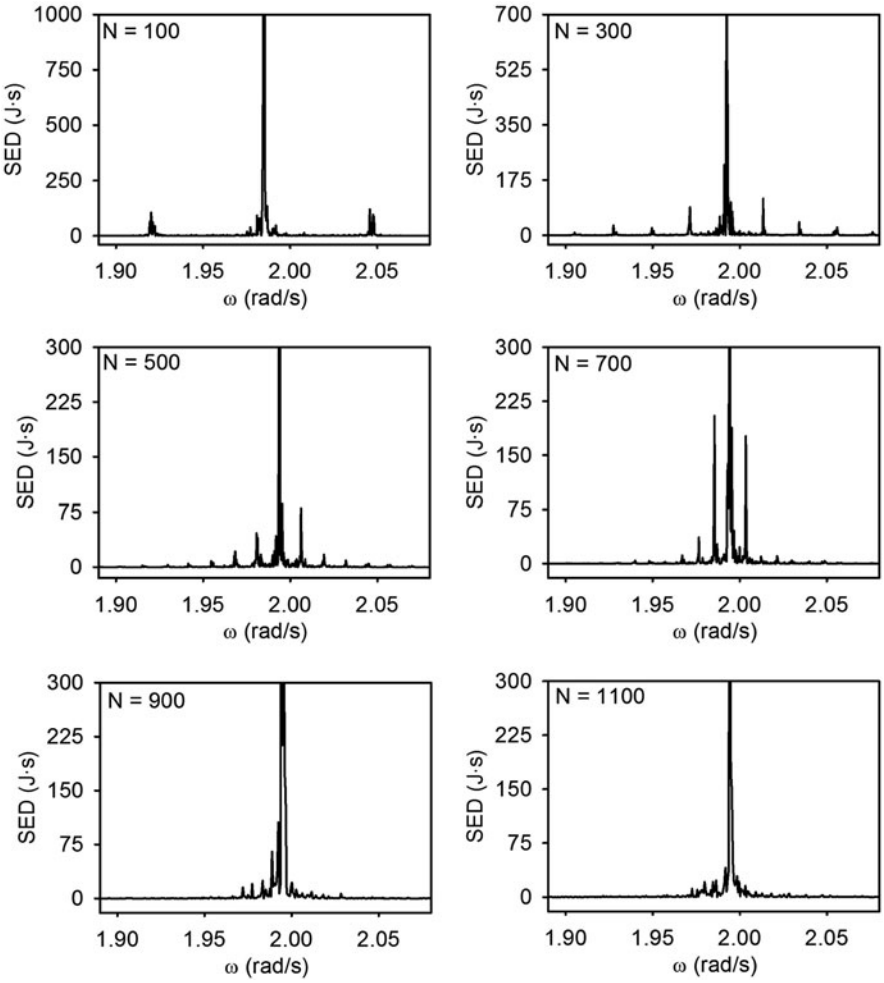

Fig. 9.7 SED-frequency plots for 1D anharmonic monoatomic crystal at $k = \pi/a$ for MD systems of varying sizes. The parameter characterizing the degree of anharmonicity in the 1D crystal is $\varepsilon = 3.0$

and circles, displacement values are 5 % and 2 %, respectively. Quadratic dependence is observed for values of ε ranging from 0.0 to 3.7. Beyond $\varepsilon = 3.7$, the potential energy function becomes completely unstable.

Analysis of the weakly anharmonic 1D monoatomic crystal has shown that the lifetime of phonon modes is not significantly affected by nonlinear interaction forces because it is pathologically difficult to satisfy the conditions for frequency and wave vector conservation. On the contrary, there exist conditions between short wavelength phonons and long wavelength phonons whereby near-resonance peaks emerge in plots of SED-frequency spectra. Satellite peaks materialize when the

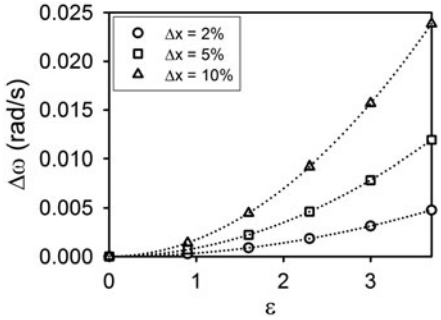

Fig. 9.8 Frequency-shift evaluated at $k = \pi/a$ for 1D anharmonic crystal relative to harmonic case. *Symbols* represent different magnitudes for the maximum initial random displacement imposed upon the masses in the 1D crystal in terms of percentage of the lattice spacing. *Circle*, *square*, and *triangle symbols* represent small, intermediate, and large initial displacements, respectively

anharmonicity of the system is adequately sampled. Lastly, nonlinear interaction forces lead to amplitude-dependent frequency shifts.

9.2.4 Anharmonic One-Dimensional Superlattices

In this section, the insight gained from analysis of the 1D harmonic and anharmonic crystals is extended to a series of superlattice configurations. A characteristic feature offered by periodic media is folded phononic band structures. Band-folding allows the conditions for wave vector and frequency conservation to be easily satisfied thereby greatly impacting three phonon processes because a greater number of phonon mode decay channels are available. Three direct consequences of band folding are (1) modulated eigenfrequencies for vibrational modes, (2) decreased phonon mode group velocities, and (3) altered phonon mode lifetimes. The superlattice configurations considered in this section do not possess the ability to boundary-scatter phonons because the potential describing the interaction between particles of differing mass is identical to the potential between particles of the same mass. Accordingly, the discussion of phonon mode lifetime is limited to coherent, band-folding effects. The main objective in this section is to illustrate the role superlattice periodicity plays in modulating eigenfrequencies and phonon mode lifetimes at a constant filling fraction. For all superlattices considered, the total number of atoms simulated with MD is $N = 800$. Every plot presented represents an average over a minimum of five unique MD simulations with randomly generated initial conditions. For superlattice unit cells, the mass of the black atom amounts to 50 % of that of the white atom.

To begin with, consider the 1D anharmonic diatomic crystal (superlattice 1:1) as pictured in Fig. 9.9. In comparison to the 1D anharmonic monoatomic crystal, a single fold in the phononic band structure occurs at wave vector mode $k = \pi/2a$.

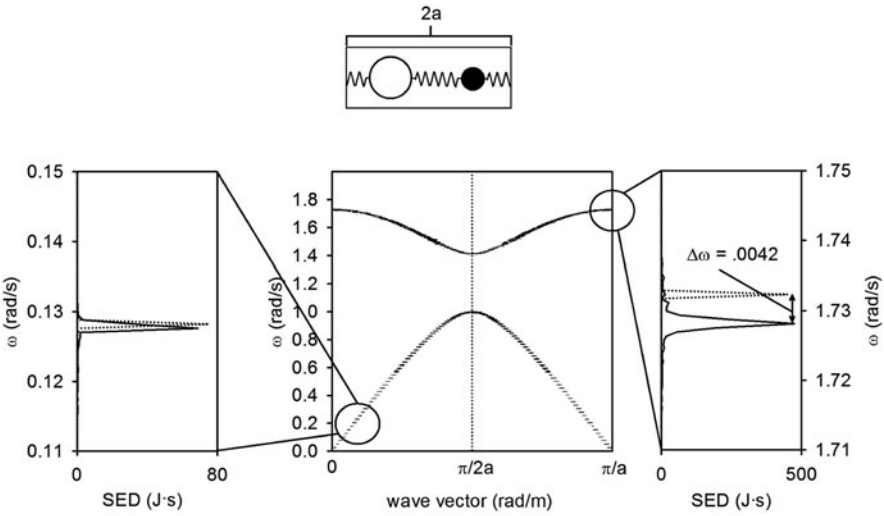

Fig. 9.9 (*Top*) unit cell for diatomic crystal. (*Center*) band structure for 1D anharmonic diatomic crystal. (*Left*) SED-frequency plot at $k = \pi/20a$ with peaks for harmonic (*dashed line*) and anharmonic (*solid line*) cases. (*Right*) SED-frequency plot at $k = \pi/a$ with peaks for harmonic (*dashed line*) and anharmonic (*solid line*) cases

Similar to the monoatomic case, there is a region in the band structure where frequency varies linearly with wave vector. In Fig. 9.9 (right), a SED-frequency plot is highlighted at $k = \pi/a$. This mode, minus a reciprocal space vector, is identical to the mode at the center of the irreducible Brillouin zone. Two peaks are visible in this plot: the dashed line represents a peak for the 1D harmonic diatomic crystal whereas the solid line represents the anharmonic case. There is a noticeable frequency shift as well as a marked difference in peak breadth. Peak broadening is directly associated with satisfaction of conservation of wave vector and frequency conditions; the addition of a second band in the band structure allows these conditions to be met more easily. In the left hand plot of Fig. 9.9, two peaks are apparent. The dashed line corresponds to the diatomic harmonic system and the solid line represents the anharmonic case. There appears to be no significant difference in peak position or width. This result was seen in the anharmonic monoatomic case for long wavelength, low-frequency wave vector modes.

Larger superlattice configurations are now considered to probe the impact superlattice periodicity has on frequency shift and phonon lifetime. In Fig. 9.10, the band structure for a superlattice configuration consisting of a unit cell comprised of two heavy atoms and two light atoms (superlattice 2:2) is displayed. Four distinct bands span the irreducible Brillouin zone. The highest frequency band shows near zero group velocity for all nondegenerate wave vector modes. A SED-frequency plot is highlighted at $k = \pi/2a$. This plot shows information for the harmonic (dashed line) and anharmonic (solid line) cases. Similar to Fig. 9.9, there is a noticeable shift in frequency and the anharmonic peak is significantly broader

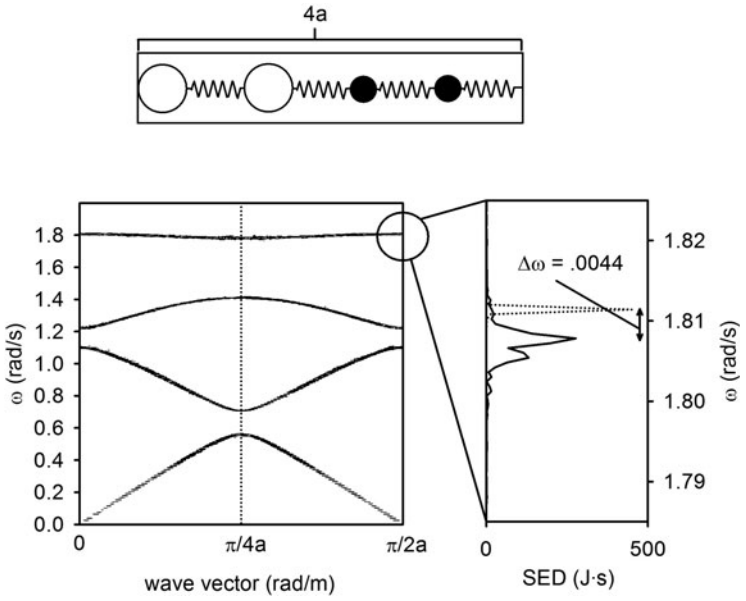

Fig. 9.10 (*Top*) four atom unit cell. (*Left*) anharmonic band structure corresponding to the four atom unit cell. (*Right*) SED-frequency plot at $k = \pi/2a$. *Dashed line* represents the harmonic case whereas the *solid line* represents the anharmonic case

than the harmonic peak. In comparison to the diatomic case, the increased number of bands in the irreducible Brillouin zone allows the conditions for conservation of wave vector and frequency to be met with greater ease. That is, many more three phonon processes satisfy those conditions. Accordingly, the anharmonic peak here shows greater width than the anharmonic peak in the right hand plot of Fig. 9.9.

In Fig. 9.11, the band structure for a superlattice configuration comprised of eight atoms (superlattice 4:4) is displayed. Eight distinct bands span the irreducible Brillouin zone. Of these bands, several show wave vector modes with near zero group velocity. The SED-frequency plot on the right hand side of Fig. 9.11 shows a very wide peak for the anharmonic case. From Figs. 9.9–9.11 it is apparent that anharmonic SED-frequency peaks broaden as the number of bands spanning the irreducible Brillouin zone increases. Accordingly, phonon mode lifetime is significantly reduced by the number of bands available. If the bands spanning the irreducible Brillouin zone are flat bands, then this effect becomes even more pronounced because for a flat band, the conditions for conservation of wave vector can always be satisfied.

With this notion in mind, a final configuration is introduced (Fig. 9.12) with superlattice periodicity 16a (superlattice 8:8). Similar to Figs. 9.9, 9.10, 9.11, Fig. 9.12 shows a frequency shift and peak broadening for the highest frequency anharmonic mode at $k = \pi/8a$.

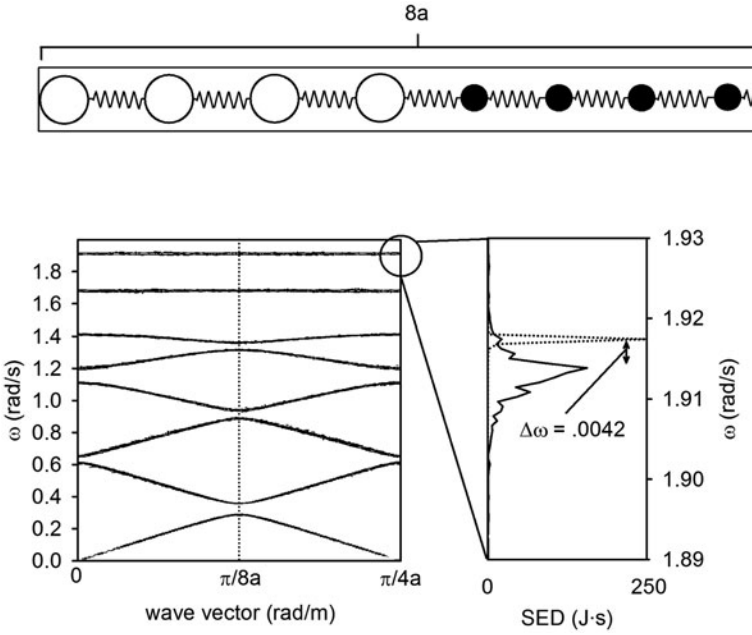

Fig. 9.11 (*Top*) eight atom unit cell. (*Left*) anharmonic band structure corresponding to the eight atom unit cell. (*Right*) SED-frequency plot at $k = \pi/4a$. *Dashed line* represents the harmonic case whereas the *solid line* represents the anharmonic case

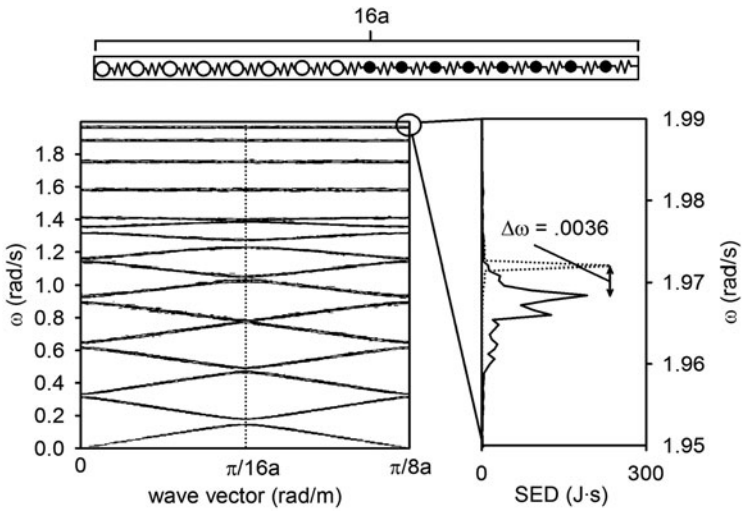

Fig. 9.12 (*Top*) 16 atom unit cell. (*Left*) anharmonic band structure corresponding to the 16 atom unit cell. (*Right*) SED-frequency plot at $k = \pi/8a$. *Dashed line* represents the harmonic case whereas the *solid line* represents the anharmonic case

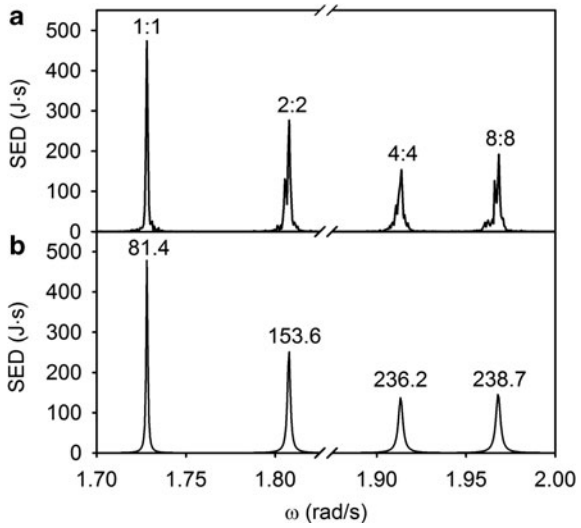

Fig. 9.13 (**a**) (*Left* to *right*) 1:1, 2:2, 4:4, and 8:8 SED-frequency plot with peaks respectively corresponding to the superlattice configurations depicted in Figs. 9.9, 9.10, 9.11, and 9.12. (**b**) Lorentzian function fits to the SED-frequency spectra in (**a**). Lorentzian peaks are labeled with half-width at half-maximum values in units of 10^{-6} Hz

To compare all four superlattice configurations, Fig. 9.13 shows (a) SED-frequency plots and (b) Lorentzian function fits to SED-frequency data corresponding to the mode with highest frequency.

Qualitatively (in Fig. 9.13a) and quantitatively (in Fig. 9.13b), it is observable that as the length of the period decreases a general narrowing occurs for anharmonic SED-frequency peaks. Accordingly, phonon mode lifetime increases when the period of the superlattice is decreased. This observation is consistent with the work presented by Garg et al. [21]. In this study it was shown that the thermal conductivity of a small period Si–Ge superlattice could be higher than that of the constituent materials. In that model, the authors calculated the thermal conductivity using the Boltzmann transport equation within the single mode relaxation time (SMRT) approximation [22]. They modeled the superlattice with harmonic and anharmonic force constants derived from density-functional theory (DFT). In that work the interfaces were treated as perfect(no boundary scattering). It was found that mass mismatch between Si and Ge atoms essentially controls phonon dispersion in the superlattices. The model also considered only three-phonon anharmonic scattering processes. Under these conditions, an increase in lifetime of the transverse acoustic (TA) modes (the majority contributors to thermal conductivity) was responsible for the observed increase in thermal conductivity of the short-period superlattice. This increase in lifetime was explained by the effect of a reduction in periodicity on the band structure of the superlattice that leads to bands that do not allow three phonon scattering events involving TA modes that satisfy the wave vector and frequency conservation rules. Additional lengthening of the phonon lifetime (and increase in thermal conductivity) was further demonstrated by changing the mass mismatch between the constituent materials.

Other authors have addressed the issue of boundary scattering in superlattices; however, these investigations have included interfacial scattering phenomena in addition to coherent band-folding effects. Experimentally and theoretically

[23–25], it has been demonstrated that phonon–boundary collisions play a leading role in decreasing the lifetime of thermal phonons in semiconductor superlattice configurations.

9.3 Phonon Propagation in Two-Dimensional Systems

Having examined the phononic properties of one-dimensional systems, we now turn our attention to two-dimensional systems. In particular, using MD we examine thermal-phonon transport in nanostructured graphene and boron nitride (BN). Both systems are technologically important materials and are characterized by large Debye temperatures; consequently they display distinct harmonic (at low temperatures) and anharmonic regimes, thereby lending themselves well to the study of phonon propagation as a function of temperature and the underlying nanostructure. Specifically, we focus on graphene sheets nanostructured with periodic antidots and boron nitride nanoribbons with aperiodic, spatially asymmetric nanoscale-triangular defects [26]. These contrasting 2D systems, which can also be experimentally synthesized, provide avenues to compare and distinguish the competition between coherent and incoherent phonon scattering and boundary scattering.

The Brenner-Tersoff style potentials [27] are invoked to represent interatomic interactions in graphene and BN as they capture the many-body, covalent nature of the atomic-bonds well, and represent the phonon band structure of the two systems accurately. The Brenner-Tersoff potential includes the anharmonicity of interatomic bonds. The potential parameters for graphene and BN are given in Ref [28] and [29], respectively.

In order to characterize phonon transport in nanostructured graphene and BN, we use relative measures of material parameters such as thermal diffusivity and thermal conductivity as indirect probes to characterize thermal-phonon propagation and lifetimes; it should be noted that it is not our intention to quantify thermal conductivity as well as diffusivity. While in principle the SED method can be invoked for such studies, the mode-by-mode analysis becomes an extremely cumbersome task involving the identification and characterization of the many phonon modes that appear due to the folding of bands within the mini-Brillouin zone corresponding to the periodicity of the phononic crystal.

Strategies to evaluate thermal conductivity and diffusivity include nonequilibrium MD (NEMD) and equilibrium MD (EMD) methods. In the NEMD framework, the thermal conductivity is obtained directly by solving Fourier's law under steady-state conditions, where a temperature gradient is maintained across the modeled material by fixing the temperature of the two ends of the material at different temperatures. Thermal diffusivity is evaluated under transient conditions, by solving for the second-order heat equation. The EMD method is based on the Green-Kubo formulations[29], where NVE (i.e., the microcanonical ensemble) conditions are imposed on the simulated system; based on the equilibrium fluctuations in the

heat current (S), the thermal conductivity (κ) is estimated from the time-dependent heat current autocorrelation function (HCAF) as given by (9.26) and (9.27), where V and T are the volume and temperature of the system respectively [30]. The thermal diffusivity (D_{T}) can then be calculated [see (9.28)], where Cp and ρ are the specific heat and mass density respectively.

$$S(t) = \sum_i E_i v_i + \frac{1}{2} \sum_{i,j} (F_{ij} \cdot v_i) r_{ij} + \frac{1}{6} \sum_{i,j,k} (F_{ijk} \cdot v_i)(r_{ij} + r_{ik}) \tag{9.26}$$

$$\kappa = \frac{1}{3k_B V T^2} \int_0^\infty \langle S(t) \cdot S(0) \rangle \mathrm{d}t \tag{9.27}$$

$$D_{\mathrm{T}} = \frac{\kappa}{\rho C_P} \tag{9.28}$$

Here, v_i and E_i represent the velocity and energy of an atom I respectively, while F_{ij} and F_{ijk} represent two body and three-body forces on atom i, due to neighboring atoms j and k.

EMD and NEMD methods have been routinely used to model thermal transport in materials, but care has to be taken in their implementation; in particular, NEMD methods impose extraordinarily large temperature gradients across the material that may not be realized experimentally; further, as discussed by Jiang et al. [31] and as also observed by the authors of this chapter [K. Muralidharan, unpublished work (2011)], the thermostated ends induce spurious vibrational modes characteristic of the size and location of the respective thermostats, which modify the injected heat flux, leading to the possible erroneous estimation of the thermal conductivity. EMD methods, on the other hand, can yield an accurate estimate of the thermal conductivity provided the HCAF is calculated over long time-periods (typically few nanoseconds).

9.3.1 Graphene-Based Phononic Crystals

Here, we report on the thermal-phonon characteristics of antidote graphene comprised of periodic arrangements of holes in a graphene matrix. This system serves as a metaphor for nano-phononic crystal (nano-PC). The lifetime of acoustic and optical phonons is found to be highly sensitive to the filling fraction of the holes in the phononic structure as well as temperature. Results are interpreted in terms of competition between elastic scattering, inelastic phonon–phonon scattering, and boundary scattering.

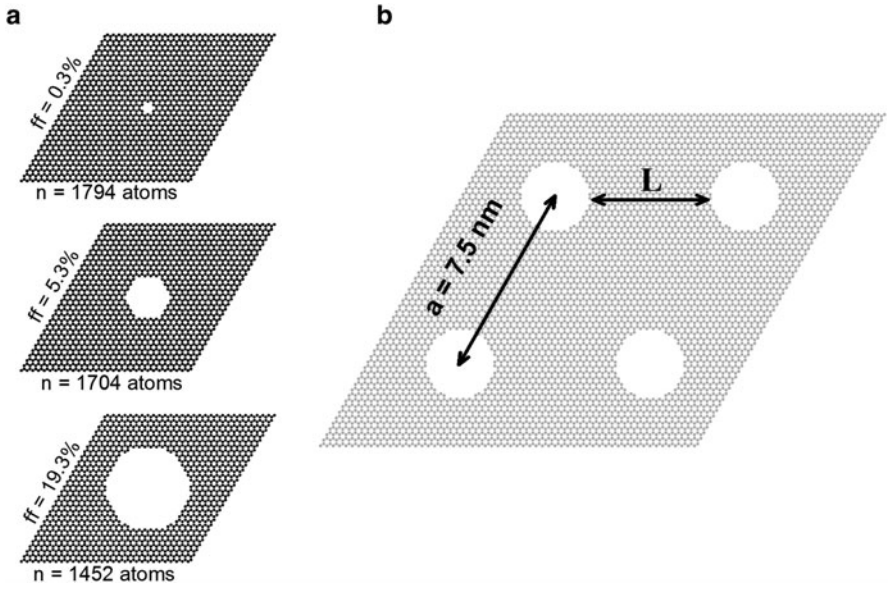

Fig. 9.14 (**a**) Three examples of unit cells for the nano-PC at different filling fraction. (**b**) an extended zone representation of the nano-PC with parameter (L), characteristic length, highlighted

9.3.1.1 Simulation Procedure

The nano-PC system of interest is comprised of a graphene matrix with periodically spaced holes. The holes are arranged in a triangular lattice with fixed lattice spacing $a = 7.5$ nm. The radius of the holes varies in size to yield a series of nano-PC unit cells with different filling fractions. Filling fraction (ff) is defined as the atomic fraction of number of atoms removed divided by total number of atoms available. In this study, filling fraction values range from 0.055 % to 20 %. Over this range, EMD calculations using the Green-Kubo method [29] are carried out to extract information on the lifetime of acoustic and optical phonons as a function of temperature (100, 300, 500 K). In Fig. 9.14a, several examples of unit cells for the nano-PC are pictured. A unit cell with ff = 0.0 % represents perfect graphene and contains 1,800 carbon atoms. Two-dimensional PBC are applied with no restrictions in the third dimension. PBC for finite-sized MD simulation cells may constrain some of long-wavelength phonon modes. For every filling fraction, a characteristic length or minimum feature length (L) is identified and is defined as the shortest distance between edges of the holes in the periodic array of the nano-PC. Characteristic length is related to filling fraction through the following relationship: $= a\left(1 - \beta\sqrt{\text{ff}}\right); \beta = \left(\frac{2}{\pi}\right)^{0.5} \sqrt[4]{3}$.

MD simulation cells are initially equilibrated at the temperature of interest by integrating the equations of motion for one million time steps under isothermal conditions using a Berendsen thermostat [32]. Next, the MD system is simulated

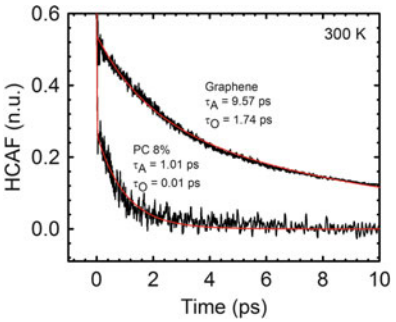

Fig. 9.15 Examples of HCAFs for graphene and nano-PC with ff = 8 %. A sum of two exponential functions is fit to the HCAF to yield estimates for average acoustic and optical phonon lifetime

under constant energy conditions for three million time steps, and the HCAF is calculated over the last two million time steps. In this work, only the last two terms in (9.26) are utilized to calculate the HCAF because these relate strictly to conduction (the convective term (first term) is neglected). Figure 9.15 shows the HCAF at 300 K for (1) perfect graphene and (2) a nano-PC with 8 % filling fraction holes.

The HCAFs exhibit two-stage decay and are, following [30], fit to the sum of two exponential functions of the following form:

$$\frac{S(t)\cdot S(0)}{3} = A_a\, \mathrm{e}^{-(t/\tau_a)} + A_o\, \mathrm{e}^{-(t/\tau_a)} \tag{9.29}$$

The longer relaxation time is assigned to acoustic modes (τ_a) and the shorter time to optical modes (τ_o). In Fig. 9.15 the average lifetimes for acoustic and optical phonons are also displayed. The decay of the HCAF is extremely rapid in comparison to perfect graphene. The nature of this decay is the subject of the remainder of this section.

The lifetime of a particular phonon mode is well described by Matthiessen's Rule:

$$\frac{1}{\tau} = \frac{1}{\tau_{\mathrm{ph}}} + \frac{1}{\tau_{\mathrm{e}}} + \frac{1}{\tau_{\mathrm{d}}} + \frac{1}{\tau_{\mathrm{B}}} \tag{9.30}$$

Here τ represents the total phonon lifetime and τ_{ph}, τ_{e}, τ_{d}, and τ_{B} signify characteristic decay times associated with different types of phonon collision processes, specifically, phonon–phonon, phonon–electron, phonon–defect, and phonon–boundary, respectively. Given the classical nature of the MD simulations, phonon–electron contributions are not included in addition to phonon–defect terms, since the MD simulation-cells are constructed to be defect free. Thus, MD simulation results are interpreted in terms of phonon–phonon and phonon–boundary scattering.

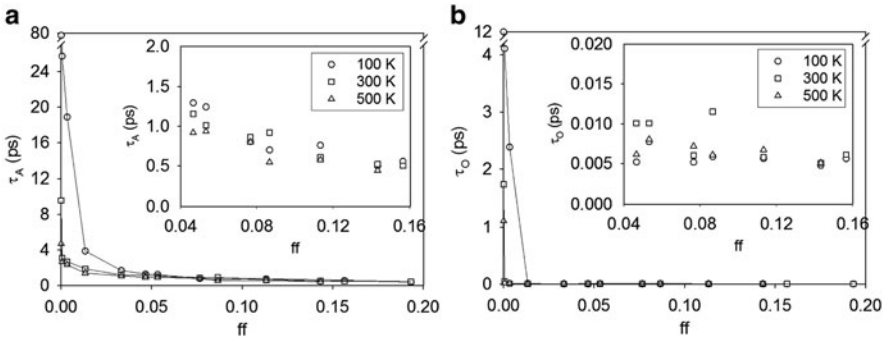

Fig. 9.16 (**a**) average lifetime of acoustic phonons versus filling fraction (100 K, 300 K, 500 K). (**b**) same as (**a**) but for optical phonons. The *insets* are magnifications of the regions of high filling fractions (ff)

9.3.1.2 Phonon–Phonon and Phonon–Boundary Scattering

Figure 9.16 shows plots of average phonon lifetime versus filling fraction of holes for acoustic phonons (a) and optical phonons (b).

For perfect graphene (ff = 0.0 %), the average lifetime of acoustic and optical phonons decreases with increasing temperature. For acoustic phonons, average lifetime decreases from 78.12 ps (100 K) to 9.57 ps (300 K) to 4.69 ps (500 K). For optical phonons, the average lifetime decreases from 11.96 ps (100 K) to 1.74 ps (300 K) to 1.10 ps (500 K). This observation highlights the phonon–phonon collision mechanism embodied in normal and Umklapp phonon processes. The calculated lifetime of optical phonons in perfect graphene at room temperature is consistent with an experimental measurement of 1.2 ps using time-resolved incoherent anti-Stokes Raman scattering [33]. Further, the predicted trend in the estimated acoustic phonon lifetimes matches experimental observations; specifically, using the experimentally measured phonon coherence length in suspended graphene (approximately 800 nm at 300 K [34–37] and 330–400 nm at 400 K [38]) in conjunction with the longitudinal acoustic velocity in graphene (approximately 20,000 m/s [39]), we obtain lifetimes that range between 15 ps (at 400 K) and 40 ps (at 300 K), which compare reasonably well with our predictions.

If a single atom is removed from the MD simulation cell, a nano-PC structure effectively results with filling fraction equal to 0.05 %. Figure 9.16a, b show for all temperatures that the removal of a single atom yields a dramatic decrease in average phonon lifetime. At 100 K the average lifetime of acoustic phonons decreases by 68 %. For 300 K and 500 K, the observed decreases in average lifetime are 63 % and 49 % respectively. This abrupt decrease in phonon lifetime can be attributed to two possible mechanisms: (1) The removal of a single atom offers a superlattice configuration whereby the phononic band structure associated with perfect graphene is folded multiple times thus allowing many more phonon–phonon scattering processes that meet the conditions for conservation of wave vector and frequency, a prerequisite for phonon mode decay; (2) The removal

of a single atom creates a boundary/surface that propagating phonons can collide with. Isolating one mechanism from the other is inherently difficult because the two are both present at the same time. However, one may rewrite equation (9.30) in terms of average phonon lifetimes to highlight the dependencies of the different contributions to the total average lifetime:

$$\frac{1}{\tau} = \frac{1}{\tau_{\text{ph}}(T, L)} + \frac{1}{\tau_{\text{B}}(L)} \tag{9.31}$$

Here, we have highlighted the dependency of phonon–phonon scattering on temperature (T) as well as the band structure resulting from the periodicity of the structure (L or ff). Boundary scattering depends essentially on the minimum feature length (L) of the structure. As filling fraction increases, for all temperatures, the average lifetime of acoustic phonon modes decreases. For optical phonons, this behavior is less pronounced. For acoustic phonons in the 0.3–3 % filling fraction region, strong temperature dependence suggests that phonon–phonon collisions are the dominant scattering mechanism. The Callaway-Holland model [40, 41] identifies the propensity of a phonon mode (of wave vector k and polarization λ) to undergo normal and Umklapp scattering processes as a function of temperature and frequency:

$$1/\tau_{\text{ph}}(k, \lambda, T) = \gamma(k, \lambda) T \text{e}^{-\eta/T} \tag{9.32}$$

Here $\gamma(k, \lambda)$ contains the frequency of the specific phonon mode and η is a parameter used to match empirical data. For the purpose of this discussion, (9.32) is adapted by considering average phonon lifetimes by defining $\tau_{\text{ph}}(T)$v to represent an average over all polarization branches. We also define a frequency independent average, $\bar{\gamma}$. Equation (9.32) becomes:

$$\frac{1}{\tau_{\text{ph}}(T)} = \bar{\gamma} T \text{e}^{-\frac{\eta}{T}} \tag{9.33}$$

Figure 9.17a shows a plot of average lifetime (acoustic and optical) versus temperature for perfect graphene. Equation (9.33) is fit to the data points with $\alpha_i = 1/\bar{\gamma}\,;\ \beta_i = \eta$. This illustrates the temperature dependence of $\tau(T) \sim \tau_{\text{ph}}(T)$ in the absence of a periodic array of holes. Figure 9.17b shows a plot of average acoustic lifetime versus temperature for three different filling fractions in the 0.3–3 % range. Similar to Fig. 9.17a, (9.33) is fit to the data points and it is well correlated. This can be interpreted as resulting from the dual dependency of phonon–phonon scattering on temperature and periodicity (through band folding), that is, $\tau(T, L) \sim \tau_{\text{ph}}(T, L)$ in the case of the antidot nano-PC structures. This result also implies that $\tau_{\text{ph}} < \tau_{\text{B}}$. Therefore, in the 0.3 % - 3 % filling fraction region, phonon–phonon processes appear to be the dominant mechanism behind the lowering of phonon mode lifetimes.

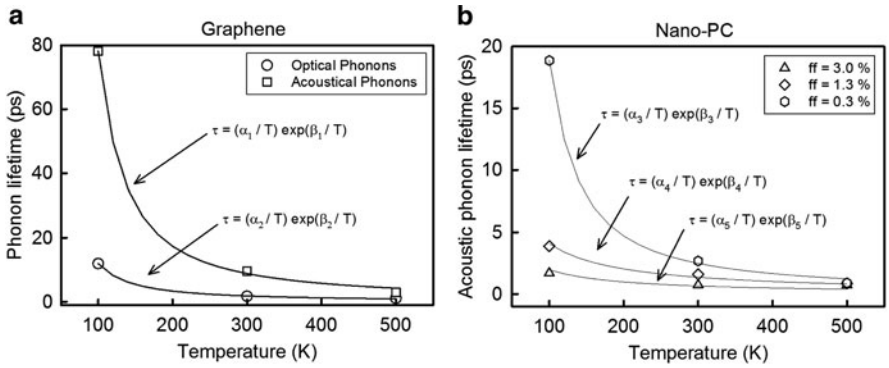

Fig. 9.17 (**a**) Lifetime versus temperature for acoustic and optical phonons in graphene.(**b**) Average acoustic phonon lifetime for three different nano-PC filling fractions versus temperature. *Symbols* are calculated values and *solid lines* represent fits using (9.33)

Beyond ff = 3.0 %, the temperature dependency of acoustic phonon lifetime is diminished. The inset in Fig. 9.16a shows, for all temperatures, that average acoustic phonon lifetime follows the same, weak linear trend as filling fraction increases. Temperature dependency of acoustic modes can be diminished if the holes in the graphene matrix have increased in size to a point whereby the characteristic length is such that acoustical phonons have higher probability of getting scattering by the boundary of a hole than with another phonon. This is the case when $\tau_B < \tau_{ph}$ and $\tau \sim \tau_B(L)$. A plot of average acoustical phonon lifetime versus characteristic length (Fig. 9.18) shows for large filling fractions (small L values) the lifetime of acoustical phonons is linearly dependent on L.

The characteristic decay time associated with boundary scattering takes the functional form [40, 41]: $\tau_B = L/v$, where v represents an average speed of sound in graphene. In the small L region of Fig. 9.18 a line is fit where $v = 7000$ m/s (a reasonable value for average speed of sound for acoustic phonons in graphene). In this region, boundary scattering is the dominant scattering mechanism. Beyond $L = 5$ nm, this linear dependence is lost and scattering is attributed to a mix of phonon–boundary and phonon–phonon collisions. As L increases to larger values, the significance of boundary scattering is lost and normal and Umklapp phonon processes dominate.

9.3.2 *Phonon Transport in Boron Nitride Nano-Ribbons*

Two-dimensional BN structures are isomorphic to their carbon counterparts and capable of demonstrating equally remarkable structure–property relations. Of particular interest are the phonon propagation characteristics in single-layer BN sheets and Boron Nitride nanoribbons (BNNR) containing triangular defects, which have been recently fabricated by Jin et al. [42]. As pointed out by Yang et al. [43], such

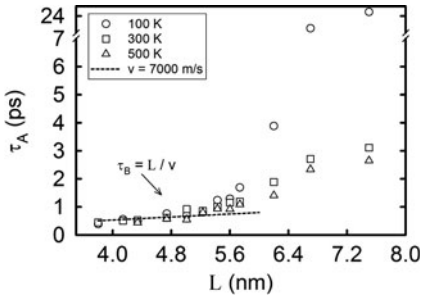

Fig. 9.18 Average acoustical phonon lifetime versus characteristic length. Phonon–boundary collisions are the dominant scattering mechanism at low L values. In this region, there is greater probability of phonon-scattering due to the hole-edge than phonon-phonon scattering

structures open up new avenues for manipulating the thermal properties of defected BNNR, and in particular, the geometric asymmetry of the triangular vacancies/defects can be exploited to preferentially scatter phonons in BNNR, which can, in turn, lead to spatially dependent thermal properties. A related consequence is the possibility of realizing thermal rectifiers as discussed by Go et al. [44], where it was shown that the thermal conductivity of a material has to be an inseparable function of both space and temperature to exhibit thermal rectification. To examine the interplay between defect-orientation and phonon propagation in BNNR, we employ (1) EMD simulations to correlate the relations between phonon transport and the temporal evolution of spatial HCAF profiles across the simulated system, and (2) a variant of NEMD simulations, where one end of the BNNR is suddenly quenched and held at a fixed temperature; the time taken for the temperature of the rest of the material to equal that of the thermostated end is taken as a measure of the thermal diffusivity and more importantly a measure of transient thermal-phonon characteristics. Note that, in both methods employed, we explicitly avoid estimating heat fluxes, and thereby circumvent problems associated with NEMD as discussed previously.

9.3.2.1 Simulation Procedure

The MD simulations of pristine and defected BNNR employ the Brenner-Tersoff potential as developed by Albe and Moller [29] due to its success in modeling the different hybridization states of BN, an important requirement while modeling defected BNNR. To ensure consistency with experimental observations [42], the arm-chair orientation of BNNR (a-BNNR) was simulated; the length of the simulated a-BNNR was 17.5 nm, while periodic boundary conditions were applied along its 7.1 nm width. Fixed boundary conditions were imposed on the edge atoms (i.e., the thinnest strip consisting of boron and nitrogen atoms at each end). For the defected system, the defect was represented by an equilateral triangle with nitrogen-termination to ensure consistency with experimental observations. The defect orientation is shown in Fig. 9.19, and its dimensions were chosen to be approximately half the BNNR width (corresponding to a filling fraction of 5 %).

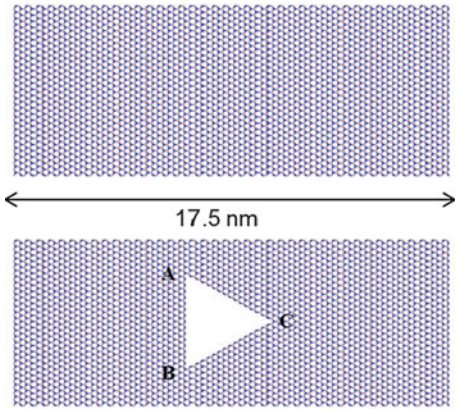

Fig. 9.19 Illustration of the pristine and defected BNNR

In order to carry out EMD simulations, both pristine as well as defected BNNR were initially equilibrated at 300 K and 900 K respectively, after which NVE simulations were conducted for 7 ns with a time step of 1 fs. The systems were spatially divided into 15 bins along their length to enable the calculations of spatial variations in HCAF, which were obtained over the last 5 ns of each NVE run. Particular attention was paid to the HCAF component along the length of the BNNR, which was primarily used in our data analysis. To ensure better statistics, five different equilibrated starting configurations were used for each case. In the NEMD simulations, the thinnest possible strip of atoms (consisting of equal number of boron and nitrogen), adjacent to the boundary atoms at the opposite ends of the BNNR, were identified to be the thermostated regions which were governed by a Nose-Hoover thermostat [32]. The boundary atoms were not included to avoid edge effects as noted by Jiang et al. [31]. For the 300 K and 900 K systems, the thermostat temperature equaled 150 K and 450 K respectively, and the time for the rest of the unconstrained system to attain the temperature of the thermostated region was calculated when the thermostat was placed at the (1) left and the (2) right edge respectively.

9.3.2.2 Phonon Transport and Rectification

The 300 K spatial variation in HCAF as a function of time for pristine BNNR is given in Fig. 9.20. Interestingly, each spatial-bin is characterized by similar, temporally periodic peaks and valleys, which are systematically displaced with respect to neighboring bins. Since the HCAF is a measure of the material's ability to dissipate thermal fluctuations, and therefore directly related to thermal-phonon energy transport, Fig. 9.20 can be interpreted in terms of phonon propagation. Specifically, the appearance of the first and the second valley in the HCAF for each bin represents phonon-reflection from the nearest and farthest fixed-edge respectively. Clearly, the time-delay between the two valleys is related to the spatial

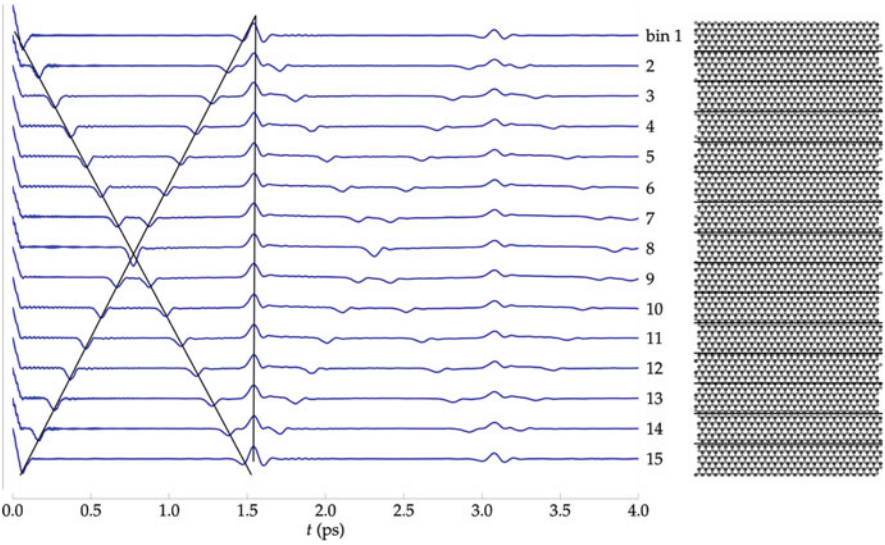

Fig. 9.20 (*Left*)- Time evolution of the spatially resolved HCAF for pristine BNNR at 300 K. Black overlays are an aid to the eye. (*Right*)-Representation of the spatial decomposition of the simulated system into 15 bins

location of the bin. Note that a single reflection from a fixed edge leads to a phase-change as represented by the valley. At approximately 1.5 ps, we see the emergence of a peak for all spatial bins. This corresponds to a 'round-trip' made by the respective phonons, which undergo two reflections (i.e., two phase changes) from either edge; the peak is larger in magnitude than the valley, representing the simultaneous arrival of the two phonons. A similar peak appears at approximately 3 ps, though the magnitude of this peak is reduced as compared to the first peak, implying the role of anharmonicity-induced scattering of phonons that eventually leads to a finite lifetime of phonons as evidenced by the gradual diminishing of the peaks and valleys in the HCAF.

While the spatially decomposed HCAF of pristine BNNR is symmetric (i.e., HCAF of nth bin and (15-*n*)th bin are similar), this is not observed for the 300 K defected BNNR, as shown in Fig. 9.21.

An inspection of Fig. 9.21 reveals that additional phonon reflection is enabled by the AB-face (see Fig. 9.19) of the triangular defect that is parallel to the BNNR edge, leading to dissimilar HCAF profiles in the two regions that are separated by the triangular vacancy in the defected BNNR.

In particular, consider the first two HCAF valleys/peaks in the bins between the triangle-face AB and the near edge (i.e., bins 1–6). The bins in proximity to the BNNR edge (bins 1–3) are characterized by valleys followed by peaks in HCAF, while the HCAFs in bins closer to the triangle-face AB (bins 4–6) are first described by peaks and subsequently by valleys. This is explained by the fact that the triangle-face AB is not a fixed boundary, and does not lead to a phase change during

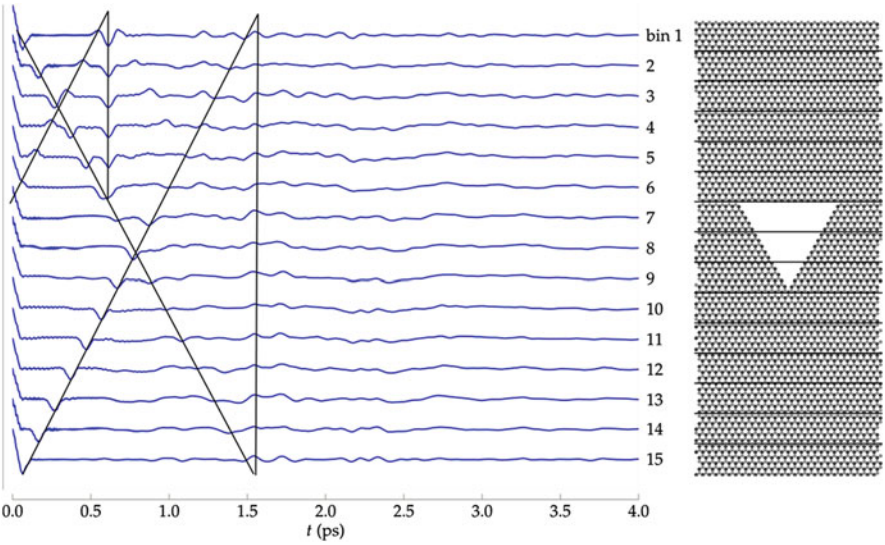

Fig. 9.21 (*Left*)- Time evolution of the spatially resolved HCAF for defected BNNR at 300 K. (*Right*)-Representation of the spatial decomposition of the simulated system into 15 bins

reflection. At approximately 0.7 ps, we see the uniform appearance of valleys for all the bins (9.1–9.6), which is correlated to the simultaneous 'round-trip' arrival of two phonons. Note that the same phenomenon is also observed in the pristine BNNR system at 1.5 ps due to the longer path (almost twice) traversed by the respective phonons. For the region in the defected BNNR between triangle vertex-C and the farther edge, the spatial HCAF profile diverges from that of the other region; all the bins corresponding to this region (9.9–9.15) are characterized by an initial valley (reflection from the farther fixed end), but subsequent features are not well pronounced, a direct consequence of phonon scattering from the sloped edges of the triangle defect, which can be distinguished from the reflection that occurs at the normal AB face. Thus, phonon propagation characteristics in the two regions separated by the geometrically asymmetric triangular defect are indeed different.

Figure 9.22a, b illustrate the HCAF of pristine and defected BNNR at 900 K. A comparison with Figs. 9.20 and 9.21 indicates the role of temperature on the HCAF profile. Clearly, the anharmonic effects become more distinct at the higher temperature, as seen by the absence of higher order HCAF echoes in the respective systems. Thus, by comparing and contrasting the HCAF characteristics of pristine and defected BNNR, one can conclude that geometric asymmetry of the defect leads to distinct spatial- and temperature-dependent thermal-phonon propagation characteristics for the defected BNNR system, indicating the possibility of observing thermal rectification in such systems.

In order to study the transient response of the two systems, the quenching procedure as described earlier was adopted. Figure 9.23a, b illustrates the rate of

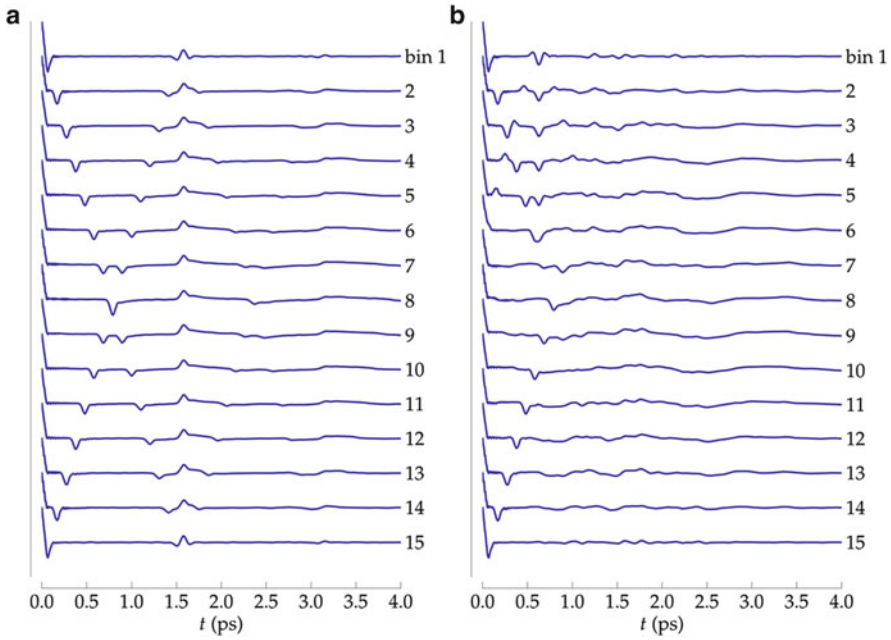

Fig. 9.22 Time evolution of the spatially resolved HCAF for (**a**) pristine and (**b**) defected BNNR at 900 K

temperature change for the pristine BNNR and defected BNNR (both initially at 300 K and quenched to 150 K), when in 'forward' bias (i.e., the thermostated BNNR edge faces the triangle-face AB) and 'reverse' bias (i.e., the thermostated BNNR edge faces the triangle vertex-C). While the pristine BNNR responds identically under both forward and reverse bias, the temperature-time curve do not overlap for the defected BNNR, implying that the thermal diffusivity is position-dependent. Numerical solution of the transient heat equation shows that the reverse-bias apparent thermal diffusivity is higher by a factor of 1.13. A similar result was also observed when the 900 K systems were quenched to 450 K, with the ratio of the reverse-bias to forward-bias thermal diffusivity for defected BNNR equaling 1.07. These results when viewed in conjunction with the HCAF observations clearly indicate that the asymmetric triangular defect plays an important part in the ability of the defected BNNR to respond to external thermal stimuli. Specifically, based on the orientation, specific triangular-faces can impede phonon-energy propagation, thereby allowing defected BNNR systems to exhibit spatially asymmetric thermal transport properties.

Importantly, these results are consistent with past theoretical and experimental investigations, where boundary scattering from arrays of spatially asymmetric triangular holes led to acoustic rectification in the MHz and GHz regimes [45, 46]. An important distinction between these studies and the current work is the explicit inclusion of anharmonic interactions that arise in atomic systems;

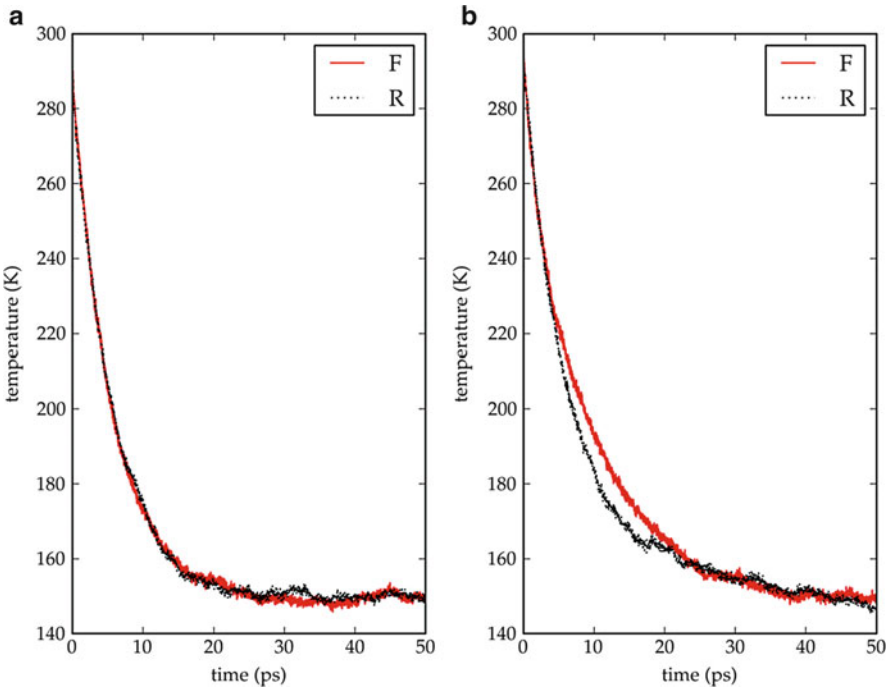

Fig. 9.23 Temperature-time plot of (**a**) pristine and (**b**) defected BNNR, when quenched from 300 to 150 K under forward (F) and reverse (R) bias

nevertheless, in each case it is clear that scattering at the triangular-hole boundary dominates phonon propagation leading to rectification. Other related atomistic investigations include the characterization of interface asperity on the in-plane thermal conductivity of superlattices [47]; here the interface asperity was represented by a series of triangles, and even the in-plane thermal-phonon transport was dictated by the surface roughness (i.e., the size and orientation of interface-triangles) further affirming the effect of boundary scattering on phonon propagation.

Acknowledgments This material is partly based upon work supported by the National Science Foundation under Grant No. 1148936 and Grant No. 0924103.

References

1. P. Hyldgaard, G. D. Mahan,"Phonon Knudsen flow in AlAs/GaAssuperlattices" in *Thermal Conductivity*, vol. 23,(Technomic, Lancaster, PA, 1996)
2. G. Chen, C.L. Tien, X. Wu, J.S. Smith, Thermal diffusivity measurement of GaAs/AlGaAs thin-film structures. J. Heat Transfer **116**, 325 (1994)

3. W.S. Capinski, H. J. Maris, Thermal conductivity of GaAs/AlAssuperlattices. Physica B **219**&**220**, 699 (1996)
4. E.S. Landry, M.I. Hussein, A.J.H. McGaughey, Complex superlattice unit cell designs for reduced thermal conductivity. Phys. Rev.B **77**, 184302 (2008)
5. A.J.H. McGaughey, M.I. Hussein, E.S. Landry, M. Kaviany, G.M. Hulbert, Phonon band structure and thermal transport correlation in a layered diatomic crystal. Phys. Rev. B **74**, 104304 (2006)
6. T. Gorishnyy, C.K. Ullal, M. Maldovan, G. Fytas, E.L. Thomas, Hypersonicphononiccrystals. Phys. Rev. Lett. **94**, 115501 (2005)
7. J.-N. Gillet, Y. Chalopin, S. Volz, Atomic-scale three-dimensional phononic crystals with a very low thermal conductivity to design crystalline thermoelectric devices. J.Heat Transfer **131**, 043206 (2009)
8. B.L. Davis, M.I. Hussein, Thermal characterization of nanoscalephononic crystals usingsupercell lattice dynamics. AIP Adv. **1**, 041701 (2011)
9. A. Netsch, A. Fleischmann, C. Enss, "Thermal conductivity in glasses with a phononic crystal like structure", PHONONS 2007. J. Phys. Conf. Ser. **92**, 012130 (2007)
10. J.-F. Robillard, K. Muralidharan, J. Bucay, P.A. Deymier, W. Beck, D. Barker, Phononic metamaterials for thermal management: an atomistic computational study. Chin. J. Phys. **49**, 448 (2011)
11. D.C. Wallace, *Thermodynamics of Crystals* (Wiley, New York, 1972)
12. D.C. Wallace, Renormalization and statistical mechanics in many-particle systems. I. Hamiltonian perturbation method. Phys. Rev. **152**, 247 (1966)
13. A.A. Maradudin, A.E. Fein, Scattering of neutrons by an anharmonic crystal. Phys. Rev. **128**, 2589 (1962)
14. R.K. Narisetti, M.J. Leamy, M.J. Ruzzene, A perturbation approach for predicting wave propagation in one-dimensional nonlinear periodic structures. ASME J. Vib. Acoust. **132**, 031001 (2010)
15. K. Manktelow, M.J. Leamy, M. Ruzzene, Multiple scales analysis of wave-wave interactions in a cubically nonlinear monoatomic chain. Nonlinear Dyn. **63**, 193 (2011)
16. N.M. Krylov, N.N. Bogoliubov, *Introduction to Nonlinear Mechanics* trans. by S. Lefshetz (Princeton U.P, Princeton, NJ, 1947)
17. I.C. Khoo, Y.K. Wang, Multiple time scale analysis of an anharmonic crystal. J. Math. Phys. **17**, 222 (1976)
18. J.M. Haile, Molecular dynamics simulation: elementarymethods. (Wiley Inter-Science , 1992)
19. J.A. Thomas, J.E. Turney, R.M. Iutzi, C.H. Amon, A.J.H. McGaughey, Predicting phonon dispersion relations and lifetimes from the spectral energy density. Phys. Rev. B **81,** 081411(R) (2010)
20. G.P. Berman, F.M. Izraileva, The Fermi-Pasta-Ulam problem: fifty years of progress. Chaos **15**, 015104 (2005)
21. J. Garg, N. Bonini, N. Marzani, High thermal conductivity in short-period superlattice. Nano Lett. **11**, 5135 (2011)
22. J.M. Ziman, *Electrons and Phonons* (Oxford University Press, London, 1960)
23. S.M. Lee, D.G. Cahill, R. Vekatasubramanian, Thermal conductivity of Si-Ge superlattices. Appl. Phys. Lett. **70**, 2957 (1997)
24. W.S. Capinski, H.J. Maris, T. Ruf, M. Cardona, K. Ploog, D.S. Latzer, Thermal-conductivity measurements of GaAs/AlAs superlattices using a picoseconds optical pump-and-probe technique. Phys. Rev. B **59**, 8105 (1999)
25. Y. Wang, X. Xu, R. Venkatasubramanian, Reduction in coherent phonon lifetime in Bi2Te3/Sb2Te3 superlattices. Appl. Phys. Lett. **93**, 113114 (2008)
26. K. Muralidharan, R.G. Erdmann, K. runge, P.A. Deymier, Asymmetric energy transport in defected boron nitride nanoribbons: Implications for thermal rectification. AIP Adv. **1**, 041703 (2011)

27. D.W. Brenner, O.A. Shenderova, J.A. Harrison, S.J. Stuart, B. Ni, S.B. Sinnott, A second-generation reactive empirical bond order (REBO) potential energy expression for hydrocarbons. J. Phys. Condens. Matter **14**, 783 (2002)
28. L. Lindsay, D. A. Broido, Optimized Tersoff and Brenner empirical potential parameters for lattice dynamics and phonon thermal transport in carbon nanotubes and graphene. Phys. Rev. B **81**, 205441 (2010)
29. K. Albe, W. Moller, Modelling of boron nitride: atomic scale simulations on thin film growth. Comput. Mater. Sci. **10**, 111 (1998)
30. A.J.H. McGaughey, M. Kaviani, Phonon transport in molecular dynamics simulations: formulation and thermal conductivity prediction. Adv. Heat Transfer **39**, 169 (2006)
31. J.-W. Jiang, J. Chen, J.-S. Wang, B. Li, Edge states induce boundary temperature jump in molecular dynamics simulations of heat conduction. Phys. Rev. B **80**, 052301 (2009)
32. D.C. Rapaport, *The Art of Molecular Dynamics Simulation* (Cambridge University Press , 1995)
33. K. Kang, D. Abdula, D.G. Cahill, M. Shim, Lifetimes of optical phonons in graphene and graphite by time-resolved incoherent anti-Stokes Raman scattering. Phys. Rev. B **81**, 165405 (2010)
34. S. Ghosh, I. Calizo, D. Teweldebrhan, E.P. Pokatilov, D.L. Nika, A.A. Balandin, W. Bao, F. Miao, C.N. Lau, Extremely high thermal conductivity of graphene: prospects for thermal management applications in nanoelectronic circuits. Appl. Phys. Lett. **92**, 151911 (2008)
35. A.A. Balandin, Thermal properties of graphene and nanostructured carbon materials. Nat. Mater. **10**, 569–581 (2011)
36. D.L. Nika, S. Ghosh, E.P. Pokatilov, A.A. Balandin, Lattice thermal conductivity of graphene flakes: comparison with bulk graphene. Appl. Phys. Lett. **94**, 203103 (2009)
37. D.L. Nika, E.P. Pokatilov, A.S. Askerov, A.A. Balandin, Phonon thermal conduction in graphene: role of Umklapp and edge roughness scattering. Phys. Rev. B **79**, 155413 (2009)
38. S. Chen, A.L. Moore, W. Cai, J.W. Suk, J. An, C. Mishra, C. Amos, C.W. Magnuson, J. Kang, L. Shi, R.S. Ruoff, Raman measurements of thermal transport in suspended monolayer graphene of variable sizes in vacuum and gaseous environments. ACS Nano **5**, 321 (2011)
39. H. Suzuura, T. Ando, Phonons and electron–phonon scattering in carbon nanotubes. Phys. Rev. B **65**, 235412 (2002)
40. J. Callaway, Model for lattice thermal conductivity at low temperatures. Phys. Rev. **113**, 1046 (1959)
41. M.G. Holland, Analysis of lattice thermal conductivity. Phys. Rev. **132**, 2461 (1963)
42. C. Jin, F. Lin, K. Suenaga, S. Iijima, Fabrication of a freestanding Boron Nitride single layer and its defect assignments. Phys. Rev. Lett. **102**, 195505 (2009)
43. K. Yang, Y. Chen, Y. Xie, X.L. Wei, T. Ouyang, J. Zhong, Effect of triangle vacancy on thermal transport in boron nitride nanoribbons. Solid State Commun. **151**, 460 (2011)
44. D.B. Go, M. Sen, On the condition for thermal rectification using bulk materials. J. Heat Transfer **132**, 1245021 (2010)
45. R. Krishnan, S. Shirota, Y. Tanaka, N. Nishiguchi, High-efficient acoustic wave rectifier. Solid State Commun. **144**, 194–197 (2007)
46. S. Danworaphong, T.A. Kelf, O. Matsuda, M. Tomoda, Y. Tanaka, N. Nishiguchi, O.B. Wright, Y. Nishijima, K. Ueno, S. Juodkazis, H. Misawa, Real-time imaging of acoustic rectification. Appl. Phys. Lett. **99**, 201910 (2011)
47. A. Rajabpour, S.M. VaezAllaei, Y. Chalopin, F. Kowsary, S. Volz, Tunable superlattice in-plane thermal conductivity based on asperity sharpness at interfaces: Beyond Ziman's model of specularity. J. Appl. Phys. **110**, 113529 (2011)